A NEW APPROACH IN TRIBOLOGICAL CHARACTERIZATION OF HIGH PERFORMANCE MATERIALS

A Thesis

by

GRANT ROBERT FOX

Submitted to the Office of Graduate Studies of
Texas A&M University
in partial fulfillment of the requirements for the degree of

MASTER OF SCIENCE

May 2009

Major Subject: Mechanical Engineering

A NEW APPROACH IN TRIBOLOGICAL CHARACTERIZATION OF HIGH PERFORMANCE MATERIALS

A Thesis

by

GRANT ROBERT FOX

Submitted to the Office of Graduate Studies of
Texas A&M University
in partial fulfillment of the requirements for the degree of

MASTER OF SCIENCE

Approved by:

Chair of Committee,	Hong Liang
Committee Members,	Timothy Jacobs
	William Charlton
Head of Department,	Dennis O'Neal

May 2009

Major Subject: Mechanical Engineering

ABSTRACT

A New Approach in Tribological Characterization of High Performance Materials.

(May 2009)

Grant Robert Fox, B.S., University of New Mexico

Chair of Advisory Committee: Dr. Hong Liang

This research conducts tribological investigation in three areas. The first area of research is to obtain basic understanding of tribological properties of high performance Inconel alloys. Pin-on-disk testing was conducted through a range of applied normal loads and sliding velocities in an unlubricated condition. Average friction coefficient, friction work, and specific wear rates were calculated from the data and microscopy techniques were used to observe and characterize wear mechanisms. Experimental results show a dependence of average coefficient of friction as a function of frictional work. Also shown is the wear rate dependence on frictional work, predicated by a wear mechanism change. This research gives a tribological baseline for high performance alloys.

The second area of research is in the in situ spatial study of friction, complemented by monitoring changes in electrical contact resistance (ECR). Pin-on-disk testing of samples was done under low normal loads and velocities. Friction and electrical contact resistance measurements were taken spatially in the wear track during each friction cycle, giving a spatial evolution of friction and resistance change, in situ. Results show a lowering in the ECR under increased friction cycles, which was closely related to a change in the friction coefficient of the material. Using surface profilometry and X-ray Photoelectron Spectroscopy, we determined that the lowering of resistance is a result of surface modification through wear and development of a friction induced conductive tribo-film. This research provides a simple method for in situ monitoring of friction and solidifies a fundamental relationship between friction and contact resistance.

The third area of research is the design of a variable force tribometer, incorporating the fundamental results demonstrated in the first two experiments. The creation of a novel testing apparatus to test materials under dynamic tribological conditions is given in detail. Simple experiments were performed on an Inconel sample and preliminary results show how dynamic normal and tangential forces affect the friction coefficient. These early results utilizing the variable force tribometer will lay the groundwork for more advanced research into the dynamic nature of friction.

DEDICATION

I would like to dedicate this thesis to my fiancée Megan Bliss, to my parents Will and Barbara Fox, and to my grandfather engineers Robert Fox and Robert Mills.

> I love the man that can smile in trouble, that can gather strength from distress, and grow brave by reflection. ‘Tis the business of little minds to shrink; but he whose heart is firm, and whose conscience approves his conduct, will pursue his principles unto death.
>
> –Thomas Paine (1776) (The American Crisis I)

ACKNOWLEDGEMENTS

I would like to think my committee chair Dr. Liang, and my committee members, Dr. Jacobs, and Dr. Charlton, for their willingness to listen and learn a few things about friction they may not have known before. I would like to express many thanks to all the members of the Liang Research Group for your support. Exceptional gratitude goes towards Rodrigo Cooper, Dr. Subrata Kundu and Ke Wang; those who took valuable time out of their research in which to help me in mine.

I would also like to thank Michel Belin, Julien Fontaine, and Jen-Luc Loubet of the Laboratory of Tribology and Systems Dynamics (LTDS) at the Central Lyon University. Their technical knowledge and expertise in tribological testing has inspired me to approach tribological characterization using non-traditional methods. Their generosity and support allowed for tribological studies to be done in a world class laboratory.

I would like to express my most sincere appreciation to my advisor Dr. Hong Liang. She has provided me with as much opportunity and experience one could possibly receive in working towards a Masters Degree. Her understanding, encouragement, constant support, and overall positive attitude are qualities that set her aside from her peers. I would like to extend my thanks to the National Science Foundation (NSF0535578), the Texas Engineering Experimental Station, and Texas A&M University for funding this research.

Great appreciation goes to my family during my time at Texas A&M. Their unyielding love and support during the numerous highs and lows has been priceless.

Dad, thanks for *always* being there as a father and an engineer. Mom, thanks for *always* listening, no matter what the topic. My deepest thanks go to my fiancée Megan Bliss. It has been a difficult time, but you've been with me every step of the way. There's no doubt that this successfully concludes the first step in our pursuit of perpetual happiness.

NOMENCLATURE

α	proportionallity
μ	Dynamic Coefficient of Friction
Ω	Ohm (electrical resistance)
AFM	Atomic Force Microscope
AISI	American Iron and Steel Institute
ASTM	American Society for Testing and Materials
cm	centimeter
COF	Coefficient of Friction
ECR	Electrical contact resistance
FCC	Face Centered Cubic
eV	electron Volt
GPa	giga pascal
m	meter
MEMS	Micro Eletro-Mechanical Systems
µm	micrometer
mm	millimeter
MPa	mega pascal
N	Newton
nm	nanometer
R_a	average surface roughness

RMS	Root Mean Square
s	second
SEM	Scanning Electron Microscopy
TEM	Transmission Electron Microscopy
UNS	Unified Numbering System
V	Volt
XPS	X-ray Photoelectron Spectroscopy

TABLE OF CONTENTS

LIST OF FIGURES

LIST OF TABLES

1. INTRODUCTION

This thesis covers three separate and distinct experimental investigations in tribological science. While all are performed using the most common ball-on-disk testing configuration, much of the similarity between experiments end there. Tribology is not an exact science. The subject of Tribology requires a diverse knowledge base from many different scientific specialties. Students of the subject can gain immense satisfaction from tackling problems requiring the application of fundamental concepts rooted in the traditional studies of science and engineering, yet it is difficult within existing schemes of study for anyone to feel fully in command of a subject dealing with interacting surfaces[1]. Tribology involves a significant amount of experimental science. In the past, progress has usually been preceded by some experiment or experimental observation [2]. One of the foremost reasons for the lack of concrete predictive modeling is that a tribosystem is made up many different variables such as contract stress, surface roughness, sliding speed, chemical environments, temperature, humidity, material type, among others. Any modification in the combination of these variables may yield completely different test results.

Two of the most widely used measures to characterize the performance of a tribosystem are friction and wear. Both friction and wear data can be highly informative to engineers and materials scientists who designing and/or evaluating an engineering system. However, they are neither unconditional nor universal behaviors. Bayer made the observation that there tends to be a tendency to assume linear relationships between wear when extrapolating design for a tribosystem[3]. Due to the complex nature of wear

---

This thesis follows the style of *Journal of Applied Physics*.

phenomena, such relationships are often nonlinear and can vary greatly between tribosystems. It has been shown that friction and wear are chaotic processes [4], and while it is possible to model the contact behavior between two materials, the interaction between the materials during the process of wear and friction is not so easily determined.

The stereotypical objective of tribology is often to minimize the two main disadvantages of solid-to-solid contact: friction and wear [5]. This statement is quite inaccurate; in automotive tires we wish to maximize the friction and minimize the wear. During the break in period of an internal combustion engine, we wish to maximize friction and wear of the piston rings and for proper seating and sealing. Finally, in the application of wax to the bottom surface of a snowboard, we wish to minimize friction and maximize wear as to impart as much wax as possible while doing as little work as possible.

Tribology deals with the synergy of any natural or engineered systems that have two pairs, liquid or solid, in contact with each other. The relative motion between these pairs makes it impossible to directly observe and predict the behavior of contact. There are tremendous challenges and areas to be explored.

1.1. Tribology: A Short History

The history of any modern-day science is often quite rich. Historical evidence is found through archaeological fact and occasional written record. The history of tribology is no different, with tribological achievements spanning the time from the beginning of mankind, to modern day. The field of tribology is relatively new, it was invented in 1966 by British physicist David Tabor[6]. The practice and fundamental aspects of Tribology are quite old. The root word “tribos” is translated from Greek to mean “rubbing”, and many early important tribological observations were made by Greek philosophers, scientists, and mechanicians. For example, in 400 B.C., Aristotle made the observation in his work *Questions Mechanicae* that friction was known as a very perceptible force and lowest for round objects[1].

Table 1 below highlights a few of the historical achievements in tribology pertinent to this research.

Table 1 History of important tribological achievements[1,7].

Tribologist	Achievement	Time Period
Early mankind	Earliest use of friction in conquest of fire through rubbing, drilling, or percussion	c. 1,000,000-11,000 years ago
Egyptian Civilization	Transport of 500 ton obelisks on sledges	c. 2400 B.C.
Greek and Romans	Focus on philosophy and science by Greek and roman cultures, use of metal bearings and lubricant.	c. 900 B.C. – A.D. 400
Leonardo da Vinci	Observation of proportionality of friction. Wear studies for development of bearing materials. Invention of rolling element bearings.	c. 1400-1600
Guillaume Amontons Charles Augustin Coulomb Leonhard Euler	Development of Laws of Friction. Coefficient of friction defined.	c. 1600-1750
Heinrich Hertz	Development of elastic body contact theory over Christmas vacation at the age of 23.	1881

1.2. Tribotesting

The development of the standardization of tribological research and experimentation was a result from a 1966 report prepared by the British Lubrication Engineering Working Group entitled *Lubrication (Tribology) Education and Research – A report on the Present Position and Industry's Needs*[8]. The report outlined significant deficiencies concerning tribological education and research; and the practical application of the science to large industry. One of biggest driving goals in the development of tribological science was an economic one. As an example, it was found that the potential savings to British industry resulting from improvements in education and research were about £515 million per annum[9].

Since the British Working Group published the famous 1966 report, many of the developments in tribological testing have been driven by industry in order to evaluate the performance of machines and machine elements like; gears, bearings (roller, ball, journal, air, etc.), valves, and lubricants. Many of the testing methods have now been standardized and are governed by strict ASTM standards. A sample of the more than one hundred ASTM standards for testing friction and wear are shown in table 2.

Table 2 Selection of ASTM Standards for friction and wear[10].

ASTM Standard	Title	Parameters Measured
G99 – 05	Standard Test Method for Wear testing with a Pin-on-disk Apparatus	Volumetric wear loss
D 2981 – 94	Test Method for Wear Life of Solid Film Lubricants in Oscillation Motion	Coefficient of friction and wear at failure
D913 – 03e1	Standard Test Method for Evaluating Degree of Resistance to Wear of Traffic Paint	Degree of substrate coverage over area of representative wear
B611 – 85	Standard Test Method for Abrasive Wear Resistance of Cemented Carbides	Abrasion resistance and wear number
D3702 – 94	Standard Test Method for Wear Rate and Coefficient of Friction of Materials in Self-Lubricated Rubbing Contact Using a Thrust Washer Testing Machine	Wear rate and coefficient of friction

The goal of most tribological testing is to determine values for frictional forces, the amount of wear and the wear mechanism. In order to fully understand the friction and wear values, the parameters used to describe friction and wear must be understood. This is critical when comparing values from different studies and testing methods. The parameters pertinent to this research will be discussed in depth below.

1.3. Friction Parameters

The first known study in the question of losses attributed to friction was published by French scientist Guillaume Amontons in 1699[1]. The results of Amontons' work with friction are known as the laws of friction, detailed below:

1. The force of friction is directly proportional to the applied load.
2. The force of friction is independent of the apparent area of contact.

Through the additional work in friction study by Charles Augustin Coulomb and Leonhard Euler the amount of friction in contacting bodies is referred to as the coefficient of friction and is represented by equation 1 below[11]:

$$\mu = \frac{F}{N} \tag{1}$$

where:

F	is frictional force acting tangential to the contact surface [N];
N	is the normal force acting normal to the contacting surface [N];
μ	is the coefficient of friction between the two bodies.

The first law has been used extensively throughout this research.

1.4. Hertzian Contact Pressure

Mechanics of materials tell us that two solid bodies in contact will deform under an applied load. This deformation will either be elastic or plastic, depending on the magnitude of the applied load and materials in contact. In many tribological applications, such as bearings, the surfaces are non-conformal and the contact areas are very small and resulting pressures very high[5]. Using relationships developed by Hertz, based on the theory of elasticity, the stress at the point of contact of the materials can be calculated. The maximum contact pressure between two bodies is often referred to as the Hertzian contact pressure. The Hertzian contact pressure is a function of the contact area a, and normal load W, reduced contact radius R', and reduced Young's modulus E'.

The relationship between these values for the standard pin-on-disk geometry in which the pin is spherical and the sample surface flat is detailed in the equations below. These equations are valid for all experiments performed in this thesis as all were done in the pin-on-disk configuration under a pure sliding condition.

The reduced radius of curvature for contact between a sphere and flat surface is shown in equation 2 below:

$$\frac{1}{R'} = \frac{2}{R_A} \tag{2}$$

where:

R' is the reduced radius of curvature [m];

R_A is the radius of the sphere [m].

The reduced Young's modulus is defined as:

$$\frac{1}{E'} = \frac{1}{2}\left[\frac{1-\nu_A{}^2}{E_A} + \frac{1-\nu_b{}^2}{E_B}\right] \tag{3}$$

where:

E' is the reduced Young's modulus [Pa];

ν_A is the Poisson's ratio of the sphere material;

ν_B is Poisson's ratio of the sample material;

E_A is Young’s modulus of the sphere material [Pa];

E_B is Young’s modulus of the sample material [Pa].

The contact area radius between pin and sample for the given geometry is calculated using equation 4 below:

$$a = \left(\frac{3WR'}{E'} \right)^{1/3} \tag{4}$$

where:

a is the radius of contact area [m];

W is the normal load [N];

R’ is the reduced radius of curvature [m];

E’ is the reduced Young’s modulus [Pa].

In tribologilical studies, the diameter of the contact area 2a, is called the semi-contact width.

The maximum Hertzian contact pressure can be calculated from equation 5 given below:

$$P_{\max} = \frac{3W}{2\pi a^2} \tag{5}$$

where:

P_{max} is the maximum Hertzian contact pressure [Pa].

1.5. Wear

Wear of materials can be defined as a progressive damage to a surface caused by relative motion with respect to another substance[12]. This broad definition of wear is meant to include traditional aspects like loss of volume in a material as well as non-tradition aspects like dimensionality change though plastic deformation and surface and subsurface cracking. There are three different ways in which wear maybe classified. The first is in terms of the wear scar present after testing. Examples of terms used to classify the wear scar are pitted, ploughed, scratched, grooved, gouged, and such. The second classification is in terms of the characteristic type of wear mechanisms. The most prevalent being adhesion, abrasion, and oxidative type wear. The third method to classify wear is in terms of wear in an engineered or test system. Engineers use examples such as lubricated wear, non-lubricated wear, pure sliding wear, and rolling wear. Often, as is the case of the experiments subject in this thesis all three categories will be used to describe the type of wear present. Of the categories described above, understanding wear mechanisms between solids is critical for an engineer as it can often influence friction behavior and induce failure. For this reason a brief explanation of wear mechanisms will be given below.

1.5.1. **Adhesive Wear**

There have not been any predictive theories quantitatively confirmed by experts for the adhesive wear of ductile materials[13]. The highest values of adhesion are often seen for a combination of like metals, but are common in all metal-to-metal contacts[5]. Additionally, high values of adhesion have been reported between metals and polymers and metals and ceramics[14]. Transfer films are the most characteristic features of adhesion, and occur when material is transferred from one surface to another. This is most evident by areas in which material has delaminated from one contacting surface. Transfer films can also appear as highly plastically deformed wear particles. Surface cracks are also evident of severe adhesive wear.

1.5.2. **Abrasive Wear**

Wear by abrasion is wear caused by contact between a particle and solid material[5]. It is typically caused when the hardness of the two testing materials vary. Hard wear particles or asperities from one surface are moved through the softer surface by the relative motion between bodies. Abrasion happens though cutting, fracture, and fatigue. Cutting is most commonly seen in ductile materials and is thought of as a sharp “grit” or hard asperity cutting the softer surface. The cut material is removed as wear debris. Cutting can take the form of microcutting by small hard grits or “ploughing” of larger grits through the surface[5]. Fracture is typically found in brittle materials in which the contact with sharpened grits causes crack formation and growth. This build up in cracking ultimately leads to the release of large quantities of material through fracture of the wear surface. Fatigue is caused by repeated strain caused by grits deforming the area on the surface. Abrasive wear happens by two modes; two-body, and three-body. Two-body abrasive wear is similar to the use of sandpaper on a surface. In which the wear producing agent is the countersurface[15]. This is usually done through hardened grits or asperities. In three-body abrasive wear the grits are allowed to freely roll and slide over the surface.

1.5.3. **Oxidative Wear**

Oxide films are present on almost all metals and will form on any clean surface exposed to oxygen even at cryogenic temperatures[5]. At high sliding speeds, oxidative wear is caused by the rapid oxidation of the metallic testing surface due to high temperatures created by friction heating between the two surfaces. Oxide layers at the highest contact spots are continuously built up and destroyed. At high sliding speeds, oxide films of several micrometers thick can build up on the worn surface[16]. At lower sliding speeds frictional temperature rises are not high enough to causes rapid oxidation at asperity tips. Oxidative wear is still prevalent but through the accreditation of pre-existing surface oxide wear debris in the worn surface.

1.6. Wear Parameters

To categorize varying levels of wear experienced at different test parameters between the surfaces of solids, a wear parameter must be defined. For this purpose the specific wear rate, k will be defined in the expression below[5]:

$$k = \frac{V}{W \times L} \qquad (6)$$

where:

k is the specific wear rate [m^3/Nm];

V is the wear volume [m^3];

W is the normal load [N];

L is the total sliding distance [m].

1.7. Frictional Study of Inconel Alloys

The properties and performance of materials in tribological applications play important roles in engineering design and evaluation. This section will focus on one of the material classes that relatively new and unique to tribology; superalloys.

The term “superalloy” was coined in the early 1940’s to describe alloys exhibiting excellent mechanical strength and creep resistance at high temperatures, and corrosion/oxidation resistance. The most commonly utilized “superalloys” today is the Inconel series of metals; a nickel based, multi-phase alloy made by Special Metals Corporation. These alloys have been used extensively in design for “extreme” engineering environments like gas turbine blades[17], experimental aircraft, nuclear reactors, steam power plants, petrochemical equipment, and other high temperature environments[18].

The most popular “superalloys” used today is the Inconel series of metals; a nickel based alloy made by Special Metals Corporation. Inconel alloys have traditionally been used in high temperature environments for their beneficial mechanical properties, but are increasingly employed in additional design situations that take into account their other beneficial mechanical properties. The least studied aspect of Inconel and its use in newer and non-traditional applications is its friction characteristics.

1.7.1. **Friction and wear**

Very few friction and wear studies have been performed on Inconel alloys. Most of the friction and wear testing that has been done is in support of very specific tribosystems.

An example is one tribosystem that experiments with Inconel alloys being chemically modified to increase the wear properties. One such system was a metal matrix-ceramic surface layer consisting of Inconel 625 modified with tungsten carbide[19]to decrease the coefficient of friction. While the end result of the experiment was a noticeable decrease in coefficient of friction (0.7 to 0.5) and reduction in the wear of the Inconel composite, it comes at the cost of significant modification of the surface (through melting) and inconsistent composite microstructure layer. Another study has recently observed the tribological performance of Inconel 718 alloy thermochemically nitrated in order to form a hardened case[20]. The modified Inconel surface showed significant coefficient of friction reduction but only for a limited amount of time.

Other Inconel wear and friction test focus on tribosystems that have been designed specifically to replicate engineered applications. On such study is in the investigation of the use of Inconel in high-temperature un-lubricated foil air bearings[21]. The tribosystem involves contact between the foil and journal surfaces only at start-up and shut down and therefore friction and wear data is defined under very specific conditions and variables. Studies on the friction and wear of Inconel 690 and 600 series of alloys have been done to characterize fretting damage caused by excessive vibration in nuclear reactor cooling tubes[22]. These tests were done at room temperature and in an aqueous environment to simulate the specific real world conditions.

Few generalized tribological studies of Inconel have been done despite its increased use as a high performance engineering material in widespread operating environments. The Inconel wear studies that have been done are either highly constrained and involve significant modification to the alloy, or are applicable to a very specific engineered system or as a direct result of an engineered system failing to work as expected. An in depth understanding of the basic friction and wear characteristics of these types of materials have yet to be achieved. In the present study, we will conduct a dynamic friction and wear evaluation of two Inconel alloys.

1.8. Frictional Studies of Micro-materials

As detailed above, the wear of engineering materials in practical applications has been studied for centuries. There are many examples of early civilizations that developed bearings and low friction surfaces as shown in table 1. The most common modes of wear studied in contacting surfaces are abrasion and adhesion, however, as science and engineering moves to a smaller scale, traditional methods and analyses used to characterize wear are not sufficient.

At the micro levels, contact kinetics between various mechanical interfaces in micro electro-mechanical system (MEMS) elements becomes very important and a great deal of research is ongoing to understand the predominant issues; stiction and friction.

Sticiton is a term used to describe the unintentional adhesion of surface microstructures through interfacial forces such as capillary, chemical, Van der Waals, and electrostatic attractions[23]. Often in MEMS in which surface area to volume ratios are very great and resultant surface energies high; coupled with the fact that resistive forces (friction, surface tension) which scale with area, are a 1000 times less than those proportional to volume (inertial, electromagnetic forces), interfacial forces are large enough to prevent motion by the mechanical system[24].

Friction and the associated wear between two contacting surfaces also play an important role in the successful operation of MEM systems. When manufactured at the micro level, extremely tight tolerances are necessary for the precise and consistent operation of a MEM system. As an example, the physical interface between rotor and hub flange on a micro stepper motor results in significant friction and wear during operation, the result of which limits the repeatability of operation[25].

The aspects of stiction and friction, and their relationship with the mechanisms involved in structural failure have not yet been fully understood. The extent to which a MEM system experiences structural failure as a result of friction and wear is unknown. Questions have arisen about the relationship between structural failure and surface wear of the MEM components[26].

1.8.1. **In Situ Wear Testing**

Attempts have been made to experimentally detect the wear in situ, both at the macro, micro, and nano levels.

The most current in situ wear studies of materials at all levels focus on the study of wear debris as it is generated, often through high-resolution microscopy. In one such study by Wang, the wear particles generated from a carbon nitride surface are studied using a Scanning Electron Microscope (SEM) as the surface undergoes repeated sliding contact against a diamond tip[27]. This method is extremely beneficial as compared to last cycle wear examination due to the chaotic nature of wear. Only in situ examination can provide direct evidence, rather than inferring how, when, and wear particles are generate during the cycle[27].

In application specifically to MEMS, a micro-tribological laboratory is in development at Sandia National Laboratory that fits on an integrated circuit chip. The laboratory will have the ability to accurately and verifiably measure mechanical properties across an entire MEMS wafer [28]. While this approach may prove successful in characterizing certain micro-tribological aspects of MEMS, the results are highly constrained to functionally specific MEMS surface interactions. Additionally, few publications have been made as to the nature of the results of the micro-tribological laboratory.

Tribology is also being investigated in situ at nano levels. In a recent study, in situ characterization using transmission electron microscopy (TEM) observed the metal-to-metal adhesive contact behavior between a tungsten probe and gold sample[29]. Our research group has also reported in situ monitoring of the wear characteristics of materials at the nano scale. A current publication spotlights evidence of the nanoabrasive behavior of silicon after nano indention and scratching as shown by an in situ atomic force microscope (AFM)[30]. These studies have highlighted the real-time examination of tribological characteristics like adhesion, nanoabrasion and ploughing wear mechanisms and effects of contamination at the nano scale.

The largest problem with in situ wear monitoring at the micro/macro scale is that while instantaneous monitoring can be accomplished, we do not have the ability to monitor the in situ evolution of said wear. Additionally, the nature of sliding contact between samples cannot be optically measured, so additional methods of measurement are needed. We propose an in situ approach to study the evolution of surface and interface phenomena during friction and wear. In order to be able to precisely detect these surfaces and interfaces, we have designed samples that are textured with two different materials having completely different mechanical and tribological properties. We make use of an approach using coefficient of friction and electrical contact resistance measurement to observe the instantaneous surface change under sliding contact. This technique is able to compare instantaneous spatially resolved values of coefficient of friction and electrical contact resistance in the wear track to subsequent ones. This would effectively give a friction or resistance evolution “map” by the end of the test. The understanding of friction and resistance evolution between two surfaces will bring insight from the wear behavior of small structures such as MEMS.

2. MOTIVATION AND OBJECTIVES

As summarized in section 1, recent developments in materials have challenged the advancement of traditional tribotesting. To meet the demand in a new generation materials that have multi-phases, multi-properties, and multi-functions, new approaches are needed for adequate materials evaluation, selection, design, and testing. The present research will contribute in three areas. The first will focus on the tribological characterization of Inconel, high-performance alloys. The second will be in developing a methodology for tribological testing. In situ, dynamic, and spatial consideration will be focused on. The third objective is to apply the knowledge learned from the first two experiments to develop a novel tribometer testing method. Details are discussed in the following paragraphs.

The first objective of this research is to create a tribological performance baseline for two common and inexpensive Inconel alloys, as well as to understand the wear behavior under various tribological conditions. To accomplish this, the alloys will be tested in a standard pin-on-disk contact condition on a commercially available tribometer under a range of sliding velocity and normal load conditions. The knowledge gained from this portion will assist the design of experiments for next steps.

Inconel superalloys have been used since their creation in the 1940’s for many advanced and one-of-a-kind engineering designs. The materials’ favorable mechanical properties, high temperature stability, and resistance to corrosion have made them appeal to engineers for use in specialty designs in which high temperature high strength is necessary. The features mentioned have also made Inconel alloys appealing as specialized tribo-materials. The tribosystem that Inconel alloys have been tested and designed for historically involve very high temperatures and very fast contact speeds. For this reason most of the past tribology research has been focused in this area.

The second objective of this research is to develop a methodology to characterize, for the first time, the dynamic nature of friction through in situ observation. To do so, we propose to use electrical contact resistance as a simple technique to monitor the instantaneous change in coefficient of friction of a sample during sliding contact. To do this we have designed two simple samples, which have precise micro scale geometry.

The third objective of this research is in combination of the first two; to design a novel tribometer that allows for the in situ monitoring of electrical contact resistance (ECR) while varying the applied load. Previous research by T. Tamai has shown a relationship exists between the coefficient of friction and ECR, through the true contact area of two solids[31]. Since the true contact area is can be changed with applied load, the ECR has been could be an added way to monitor change from these effects. A fundamental understand of friction and its effects on the sample can be studied utilizing this novel test machine. To meet this objective we will design an experimental setup that adapts to an existing CSM tribometer that allows for variable loading control.

The proposed research will have significant impacts on science and technology. The research will promote new concepts of dynamic friction with spatial considerations that have not been reported before. The research will be applicable to manufacturing and many areas of engineering. Particularly, the outcome of the research will directly benefit

MEMS design and fabrication that will have reduced stiction. The composite friction ideas will be important for the design dynamic friction systems such as in NASA’s Crew Exploration Vehicle. Details will be discussed at the end of the thesis.

3. MATERIALS AND EXPERIMENTAL CONDITIONS

This section describes the materials and sample preparation for this research. The characterization and testing methodology will also be detailed. The section is divided in two parts. The first part focuses on Inconel material and the second part on a material with patterned structure.

3.1. Inconel

3.1.1. **Materials**

In this study, we characterized the friction between a stainless steel pin and Inconel disk. Inconel alloy 625 and alloy HX were chosen as counter-faces for their wide spread applications in industry and ease of procurement. Inconel is a nickel-chromium-iron based alloy used in high stress, temperature, and corrosive environments. Common applications include gas turbine blades. It has a solid-solution matrix stiffened face centered cubic (FCC) crystal structure[32]. Table 3 lists the elements and composition of Inconel 625 alloy. Table 4 lists the elements and composition of Inconel HX alloy.

Table 3 Chemical composition of Inconel alloy 625[33].

Element	% Composition
Nickel	58.0
Chromium	20.0-23.0
Iron	5.0
Molybdenum	8-10
Niobium+Tantalum	3.15-4.15
Carbon	0.10
Manganese	0.5
Silicon	0.05
Phosphorus	0.015
Sulfur	0.015
Aluminum	0.40
Titanium	0.40
Cobalt	1.0

Table 4 Chemical composition of Inconel alloy HX[34].

Element	% Composition
Nickel	Balance
Chromium	20.5-23.0
Iron	17.0-20.0
Molybdenum	8-10
Carbon	0.05-0.15
Manganese	1.0
Silicon	1.0
Phosphorus	0.04
Sulfur	0.03
Tungsten	0.2-1.0
Cobalt	0.5-2.5

The pin material selected for this research was a grade three, 6 mm AISI 440C stainless steel ball. The AISI 440C martensitic stainless steel ball was chosen for its common and well characterized use in wear experiments. The grade three AISI 440 balls were ideal for testing due to their high spherical roundness and low surface roughness. Also, in bearing form, the balls are hardened to a level much higher the Inconel alloys. Additionally, martensitic stainless steels have found applications in many areas of engineering, including gas turbine engines, turbine blades, tools, bearings, and cutlery, where wear performance plays an in important role in determining the service behavior of the components[35]. Table 5 lists some mechanical properties of the materials to be studied.

Table 5 Selected mechanical properties for the different types of materials used in this Inconel research[33,34,36].

Material	Density (g/cc)	Poisson's Ratio	Young's Modulus (GPa)	Hardness
AISI 440C Stainless Steel	7.8	0.293[37]	200	58 – 65 RC
Inconel alloy 625	8.44	0.278	207.5	145-220 B
Inconel alloy HX	8.2	0.32	205	90 RB

Note: All values at room temperature. RC = Rockwell C, RB = Rockwell B, B = Brinell.

3.1.2. Sample Preparation

The samples used in these experiments were both obtained as 38mm (1.5”) bar stock from McMaster Carr. The material was received in 76.2 mm (2”) sections of the bar stock and multiple test samples were cut using a Buehler diamond saw. The width of the samples was approximately 6 mm (1/4”). To ensure parallelism, each sample was then fixed in a lathe using precision parallel bars, and both sides of the sample were machined.

After the samples were machined for parallelism, they were polished by hand on a Buehler hand polisher. A submicron finish was achieved using a progressively finer series of Buehler CARBIMET silicon carbide grinding papers. The polishing regiment consisted of ten minutes of wet hand polishing at 300, 400, 600, 800, 1000, and 1200 grit papers. Between each polishing stage, the samples were cleaned with water.

An acceptable roughness for most engineering applications is typically 0.40 µm[38]. After polishing, surface roughness readings of each sample were taken in four different locations of the sample using a Qualitest TR200 stylus surface profilometer. The average surface roughness are listed in the table 6 below and are reported as the arithmetic mean of the absolute values of profile deviation from the mean within sampling length (R_a). The number indicates each polishing step:

Table 6 Profilometer readings of Inconel samples.

Material	R_{a1}	R_{a2}	R_{a3}	R_{a4}
Inconel 625	0.23±0.02	0.17±0.02	0.19±0.02	0.59±0.06
Inconel HX	0.14±0.01	0.20±0.02	0.05±0.01	0.57±0.06

3.1.3. **Surface Characterization**

3.1.3.1. **Profilometer**

Surface roughness testing was done utilizing a Qualitest TR200 handheld roughness tester. The Qualitest TR200 roughness tester utilizes a sharpened diamond stylus mounted on a retractable probe. The roughness tester is placed on the sample and leveled. Upon measurement, the probe is mechanically pulled across the sample surface tracing the surface profile with the diamond stylus tip. Changes in the vertical distance of the probe tip is measured by an inductance circuit in the profilometer and translated to a surface displacement using the instruments onboard computer processor. Additionally, an average surface roughness for the sample is calculated. The average surface roughness is the arithmetic mean of the absolute values of surface profile deviation from a line within sampling length. The Qualtest TR200 instrument is shown in figure 1.

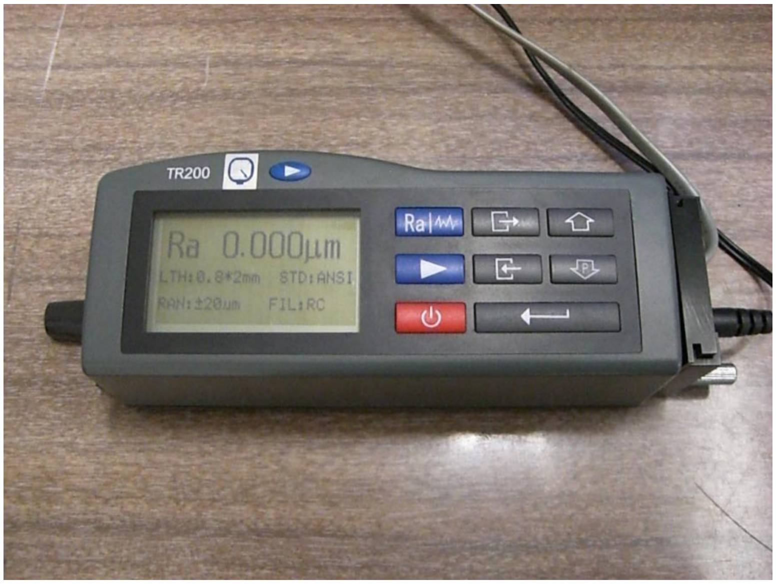

Figure 1 Qualtest TR200 stylus profilometer

.

3.1.3.2. **Optical Microscopy**

Optical microscopy of the samples was done using the Keyence VHX-600 Digital Microscope. The microscope utilized a 54-megapixel charge-coupled device camera to provide high resolutions images at high magnifications. For this research the last cycle wear tracks were examined at optical magnifications of 100 and 500X. Each wear track was examined post testing and representative wear morphology is analyzed. The Keyence microscope is also able to make length measurements on a sample image using built in software. The Keyence digital microscope is shown in figure 2.

Figure 2 Keyence Digital Microscope

3.1.3.3. **Scanning Electron Microscopy**

When high resolution images with magnification greater than 500X was necessary, the JEOL JSM-6400 Scanning Electron Microscope (SEM) was utilized. Certain wear morphologies were examined using the JEOL SEM at magnifications between 1000X and 4000X with an accelerator voltage of 15,000 electron volts (eV). The SEM was also used in the determination of non-conductive oxide wear particles. Ceramic oxide layers have mainly ironic atomic bonds and therefore few free electrons for conductivity. Oxides will then show up in contrast to conductive metals in a SEM image. The JEOL SEM used in this experiment is shown in figure 3 below.

Figure 3 JEOL JSM-6400 Scanning Electron Microscope (SEM)[39].

3.1.4. **Ball-on-Disk Tribotesting**

The tribological properties of the samples were evaluated using a CSM Tribometer configured for ball-on-disk contact and reciprocating motion. This allows for the study of friction between a sphere and flat counter-surface as they slide against each other. The spherical ball is secured rigidly in its holder to prevent any rotation. For simplification in this thesis, “ball and holder” will be designated “pin” in future use except where explicitly noted. This allows the contact to be in pure sliding and all previous assumptions to hold true. The experiment was performed with intent to the American Society for Testing and Materials standard G99[40] for pin-on-disk wear testing. Figure 4 shows the CSM Instruments Tribometer used in this experiment.

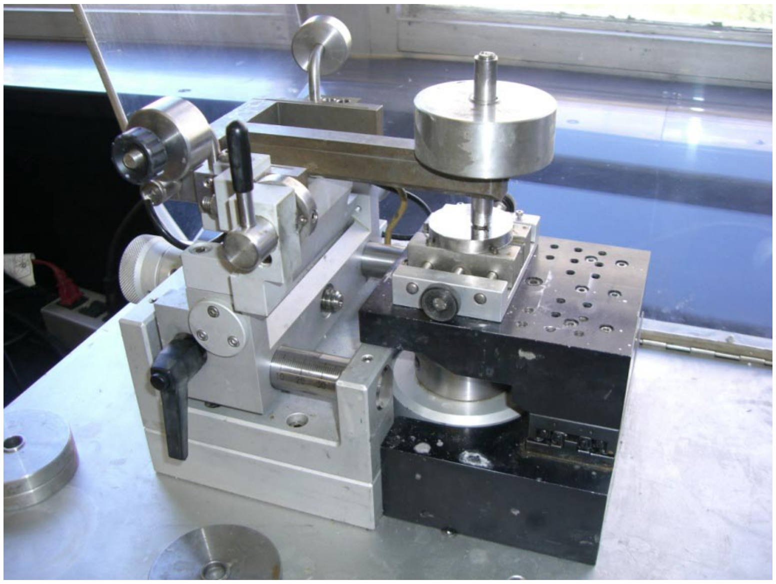

Figure 4 CSM Instruments Macro Tribometer.

The basic principle for measuring the coefficient of friction using the CSM Instruments Tribometer is as follows: The counter-surface is clamped to a fixture that undergoes speed controllable, linear reciprocation during testing. The pin is put into contact with the counter-surface and a static load is applied normal to the counter-surface to be tested. The pin is then rigidly connected to an engineered steel beam, constrained to allow linear displacement only along the direction of reciprocation. The motion of the steel beam is translated through a linear variable differential transformer as a measurable voltage change. The integral CSM Tribox software then uses the signal from the LDVT and the elastic properties of the beam, to determine the tangential force experienced by the pin. The coefficient of friction is then calculated using the proportionality equation detailed above.

Data collection and analysis was done through integrated tribology software designed by CSM Instruments. The TriboX software was used to control all the variables of testing including; counter-surface sliding speed, total sliding distance, and data acquisition rate. For further manipulation, the friction data was outputted from the TriboX software as a ".txt" format. Microsoft Excel was used to generate coefficient of friction graphs and calculate specific wear rates.

3.1.5. **Experimental Conditions**

The samples were tested in pure sliding at a range of linear velocities between 2 and 6 cm/s and a range of loads between 1N and 5N. The wear track length was 1.2 cm, and most runs were tested to a distance of 5 m. An exception to this was when testing the Inconel HX at higher loads and velocities. Beyond the applied load of 4N and the lowest velocity of 2 cm/s, adhesion between the stainless steel ball and Inconel HX disk was significant enough to cause early termination of the test. These results will not be included. The test environment was air at room temperature (24 – 28 °C), with a relative humidity of 20 – 30%. Prior to testing, all surfaces were cleaned with acetone and dried. Some important tribological properties are shown in table 7.

Table 7 Tribological data for Inconel 625 and HX samples.

Material	Load (N)	Effective Young's Modulus, E' (GPa)	Semi-Contact Width 2a (μm)	Maximum Hertzian Contact Pressure (GPa)
Inconel 625	1	221.8	60	0.43
	3		80	0.93
	4		80	1.02
	5		100	1.1
Inconel HX	1	223.5	60	0.43
	3		80	0.62
	4		80	0.68
	5		100	0.74

After the experiments, the last-cycle wear track was examined using a JEOL JSM-6400 Scanning Electron Microscope (SEM) to determine characteristic wear patterns and to analyze the wear debris. The Qualitest TR200 surface roughness tester was then used to determine wear track width. The Testing matrix for both Inconel 625 and Inconel HX is shown in tables 8 and 9 respectively.

Table 8 Test matrix for Inconel 625 experiments.

Material	Load (N)	Linear Velocity (m/s)	Approx. distance (m)
INCONEL 625	1	0.02	5
		0.03	
		0.04	
		0.05	
		0.06	
	3	0.02	
		0.03	
		0.04	
		0.05	
		0.06	
	4	0.02	
		0.03	
		0.04	
		0.05	
		0.06	
	5	0.02	
		0.03	
		0.04	
		0.05	
		0.06	

Table 9 Test matrix for Inconel HX experiments.

Material	Load (N)	Linear Velocity (m/s)	Approx. distance (m)
INCONEL 625	1	0.02	5
		0.03	
		0.04	
		0.05	
		0.06	
	3	0.02	
		0.03	
		0.04	
		0.05	
		0.06	
	4	0.02	
		0.03	
		0.04	
		N/A	
		N/A	
	5	0.02	
		N/A	
		N/A	
		N/A	
		N/A	

3.2. Materials for Micro-Friction Experiments

The experiment consisted of two types of samples. A layered metal sample was created to identify if materials constituting a composite could be observed at micro-levels by the tribometer system. The second sample consists of a composite pattern that has a structure similar to a printed silicon wafer. The materials are Ni-Si fabricated in a parallel fashion with s similar geometrical dimension. Such a simple structure makes the in situ monitoring of friction and electrical contact possible.

3.2.1. Layered Metallic Structures

The layered metal sample consisted of four metals and one polymer in a laminar structure. The metals chosen to constitute the composite were; 6061 – T6 aluminum, Copper (99% purity), UNS C36000 free-cutting brass, and 304 stainless steel. The thickness of each metal ranged between 800 and 1200 µm.

The metals were chosen for their dissimilar mechanical and tribological properties and different friction behavior. A selection of these properties is reported in table 10.

Table 10 Selected properties of metal layered sample[41],[42],[43].

Material	Density (g/cc)	Poisson's Ratio	Young's Modulus (GPa)	Hardness	μ* dry sliding
Aluminum 6061-T6	2.70	0.33	69	95 RB	0.47
Copper	8.96	0.308	110	51 RB	0.36
Brass (UNS C36000)	8.49	0.311	97	62 RB	0.44
Stainless Steel 304	8.00	0.29	200	129 V	0.57
Phenol-formaldehyde (Phenolic)			6.9	100 RM	0.78

Notes: RB = Rockwell B, V = Vickers, RM = Rockwell M. *Dry sliding coefficient is for sliding against mild steel, for comparison purposes only.

For construction of the sample, the metals were layered together and placed in a Buehler SimpliMet 1000 Automatic Mounting Press with a compression thermoset phenolic polymer, Buehler PHENOCURE. During the setting process, high pressure in the molding chamber forced the phenolic resin between the metal layers in the composite, adding a phenolic layer to the composite structure. An image of the sample is shown in figure 5.

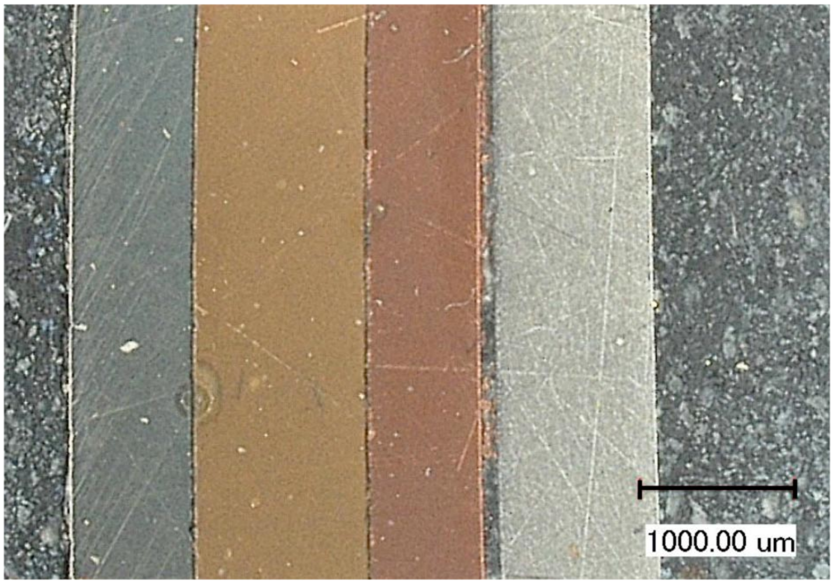

Figure 5 Metal Composite Sample at 20X magnification. Photo was taken post testing.

The spherical pin chosen for this study is an AISI 52100 steel ball of 6mm diameter. The material was chosen for its common use in industry as ball bearings; which have the benefits of high availability and acceptable manufacturing tolerances. Selected typical properties of the pin can be seen in table 11 below:

Table 11 Selected properties of pin[43].

Material	Density (g/cc)	Poisson's Ratio	Young's Modulus (GPa)	Hardness (HRC)	Electrical Resistivity (Ω– cm)
AISI 52100	7.81	0.30	210	62-66	0.0000219

3.2.2. **Ni – Si Patterned Wafer**

The experimental specimen consisted of a patterned wafer made from silicon dioxide and nickel. It was received from Semitech after a processing through chemical-mechanical polishing. The wafer surface contains strips nickel in a linear, parallel pattern. The thickness of the strips varied between 70 - 88 μm. The distance between each strip varied between 200 - 300 μm with the largest gap being 342 μm. Selected properties of the sample are shown in table 12.

Table 12 Selected properties of Ni – Si wafer[41].

Material	Density (g/cc)	Poisson's Ratio	Young's Modulus (GPa)	Electrical Resistivity (Ω – cm)
Nickel	8.902	0.31	207	0.0000064
Si – [100]	2.329	0.28	129.5	0.0010
Si – [110]			168	
Si – [111]			186.5	

Prior to testing, the surface was ultrasonically cleaned in an acetone bath for twenty minutes. For testing, the sample was mounted on an electrically conductive aluminum stage with conductive tape. Conductive silver paint was applied to the top and bottom of the sample to allow a continuous current flow through the Nickel strips. An example of the patterning is shown in figure 6.

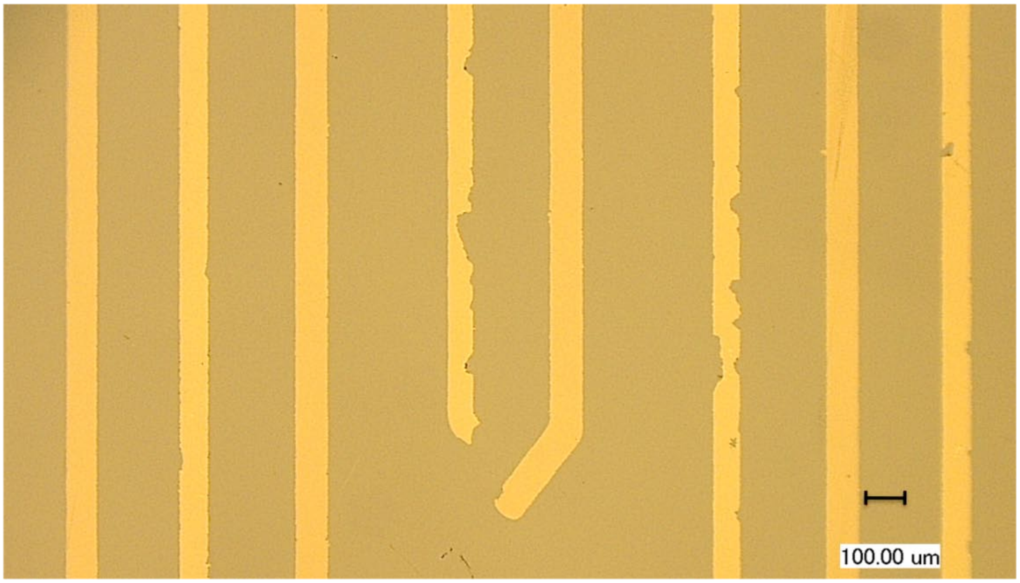

Figure 6 Nickel – Silicon wafer at 100X magnification. Damage was done previous to testing.

The spherical pin chosen for this study is an AISI 52100 steel ball of 6mm diameter. The diameter of the ball allows for a Hertzian contact area appropriate to measure the tribological performance of the relatively thin Ni strips. Properties have been previously listed in table 12.

3.2.3. **Sample Preparation**

3.2.3.1. **Preparation of Layered Metallic Sample**

After pressure casting, the entire sample was abrasively polished using a Buehuler Automet 2 auto polisher. A high polished finish was achieved using a progressively finer series of Buehler CARBIMET silicon carbide grinding papers. The polishing regiment consisted of 15 minutes of wet polishing at 400, 600, 800, 1000, 1200, and 2400 grit papers. Between each polishing stage, the samples were cleaned with water. A finishing hand polished was done using a 10μm diamond suspension and solution of: 15wt% hydrogen peroxide 85wt% deionized water. The desired effect of the solution was to chemically mechanically planerize (CMP) the sample and minimize any topography inconsistence of the sample. The sample was fixed to an aluminum stage with conductive tape, and silver paint was applied to the top, side, and bottom of the sample completing a conductive circuit from the metal layers to the holder.

3.2.3.2. **Preparation of Ni – Si Wafer Sample**

Prior to testing, the sample was ultrasonically cleaned in an acetone bath for twenty minutes. For testing, the sample was fixed on an aluminum stage with conductive tape. Conductive silver paint was applied to the top and bottom of the sample to allow a continuous current flow through the Nickel strips.

3.2.4. Micro-Friction Characterization

3.2.4.1. X-Ray Photoelectron Spectroscopy (XPS)

XPS measurements were carried out to characterize the elemental debris in the wear track. All XPS measurements were done utilizing a Kratos Axis Ultra Imaging X-ray photoelectron spectrometer (Kratos Analytical) with monochromatic Al-K_α line (1486.7 eV, 180W). The instrument integrates a magnetic immersion lens and charge neutralization system with a spherical mirror analyzer, which provides real-time chemical state and elemental imaging using a full range of pass energies. The pressure in the spectrometer was typically 10^{-9} Torr. The incident X-ray beam was normal to the sample surface and the detector was 45° away from the incident direction.

The images were collected at the characteristic binding energy (BE) of $Ni2p_{3/2}$ (853 eV). The XPS apparatus used in the experiment is shown in figure 7.

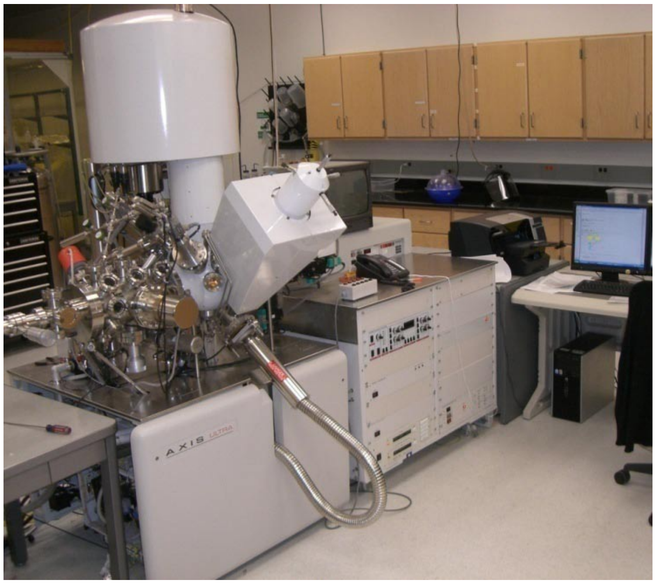

Figure 7 Kratos Axis Ultra Imaging XPS.

3.2.4.2. **3D Surface Profilometer**

To obtain high resolution three dimensional surface morphology of wear on the Ni – Si wafer, the Zygo NewView 600p phase shifting white light interferometer was used. A white light interferometer works by comparing the phase change in light that has reflected off the sample surface to a reference light. Through the analysis of constructive or destructive interference between the two light beams generated by changes in surface profile, a three dimensional surface profile can be generated. Through phase-shifting interferometry The NewView 600p is able to give less than 0.1 nm vertical resolution and 0.36 – 5.18 μm lateral resolution[44]. A picture of the instrument is shown in figure 8.

Figure 8 Zygo NewView 600p white light interferometer.

3.2.5. **Ball-on-Disk Tribotesting**

Friction measurement was done through a traditional pin-on-disk configuration to measure changes in the kinetic coefficient of friction (μ) as the wafer wears. The schematic of the tribometer is illustrated in figure 9. Determination of the coefficient of friction is made through measurements of the static load applied and tangential force experienced on the pin while the counter-surface is reciprocated beneath. The coefficient of friction is the proportionality of the tangential and normal forces.

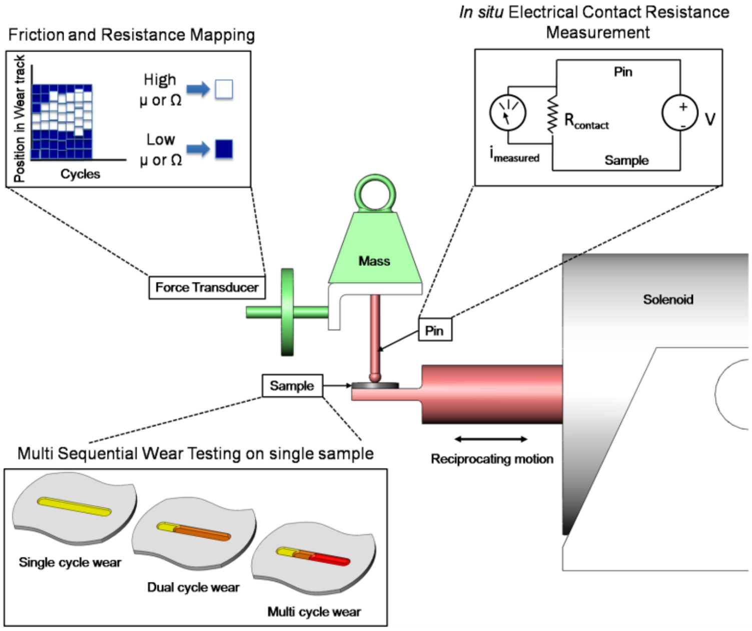

Figure 9 Schematic of tribometer system showing friction and resistance mapping, electrical contact resistance measurement and multi-sequential wear testing capabilities.

An approach was proposed to conduct friction tests while simultaneously measuring electrical contact resistance (ECR). The advantage in measuring ECR is the ability to directly observe in situ changes of the contacting surfaces. T. Tamai has shown a relationship exists between the coefficient of friction and ECR, through the true contact area of two solids[31]. Since the true contact area is constantly changing through frictional effects like surface roughness modification and oxidative films, the ECR has been proven an added way to monitor change from these effects.

The electrical contact resistance is measured through the application of a constant voltage through a circuit made up of the pin and sample. The current drop is measured across the pin/sample contact and Ohm’s law is applied to determine the ECR. This method is diagramed schematically in the upper right hand corner of figure 9. A picture of the actual tribometer is shown in figure 10 below.

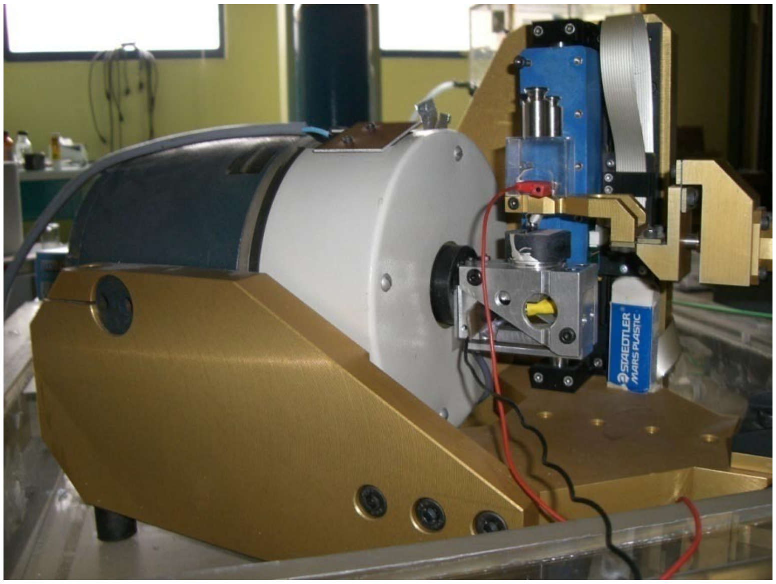

Figure 10 Tribometer system.

What differentiates the tribometer system from other techniques is the unique ability to display the spatially resolved coefficient of friction and electrical contact resistance during testing. A schematic for the spatial resolution determination algorithm is shown in the upper left hand corner of figure 9, and described in detail below. During the reciprocation of the tribometer pin, individual values for μ and ECR are sampled across 512 discrete intervals. These elements are allocated a color, based on their numerical value in a range predefined by the user. The higher values appear in color closer to white (hot), while the lower values appear in color closer to black (cold). The values are then plotted as a function of the number of cycles (x-axis) and their physical position in the wear track (y-axis). The high sampling rate is able to achieve very high graphical accuracy.

When the spatial resolution algorithm is repeated for multiple friction cycles, the results can offer insight to the development of friction and ECR change; in effect, giving a friction or ECR history map.

In addition to the mapping capability, the tribometer system also has the ability to perform multi-sequential (MSQ) wear tests. This capability is diagramed in the lower left-hand corner of figure 9. MSQ wear testing allows the experimentalist to change the amplitude of the reciprocating pin, and corresponding wear track in situ. This method allows for multiple regions of wear, in a single wear track. As a result, the associated wear morphologies can be compared and contrasted in real-time under microscopic examination, and other analytical techniques.

3.2.6. **Micro-Friction Experiment Test Plan**

Pure sliding tests were conducted in a dry un-lubricated condition, with a sliding direction perpendicular to the lamina structures in each sample. Testing was done at and

0.5 and 2 mm/s, and a load of 0.3 – 0.5N. The wear track length was 3.5 mm. The testing environment was air at room temperature (24°C), with a relative humidity of (40 – 50%). Important tribological properties for both samples are shown in tables 13 and 14.

Table 13 Tribological properties of layered metal sample.

Material (N)	Load (N)	Effective Young's Modulus, E' (GPa)	Semi-Contact Width 2a (μm)	Maximum Hertzian Contact Pressure (GPa)
Al 6061 T-6	0.3	116	40	0.28
	0.5		60	0.33
Copper	0.3	159	40	0.34
	0.5			0.41
Brass C36000	0.3	147		0.33
	0.5			0.39
304 SS	0.3	224		0.43
	0.5			0.51
Phenolic	0.3	N/A		N/A
	0.5			N/A

Table 14 Tribological properties of Ni – Si experimental wafer.

Material (N)	Load (N)	Effective Young’s Modulus, E’ (GPa)	Semi-Contact Width 2a (μm)	Maximum Hertzian Contact Pressure (GPa)
Nickel	0.3	229.9	40	0.44
	0.5			0.52
Silicon	0.3	159.6		0.35
	0.5			0.41

*calculations done using Pure Si E = 112.4 Gpa

After the experiments, the last-cycle wear track was examined using the Keyence Digital Microscope to determine characteristic wear patterns and to analyze the wear debris. The Zygo NewView 600p white light interferometer was surface roughness tester was then used to precisely determine the wear track surface roughness. XPS was used for elemental analysis of the wear track. The testing matrix for the micro-friction experiment is shown in table 15.

Table 15 Testing matrix for micro-friction experiment.

Material	Load (N)	Speed (mm/s)	Number of wear cycles	Multi-Sequential wear cycles
Layered Metal Sample	0.3	0.5	200	--
		2.0	200	--
	0.5	2.0	200	--
			200	--
			100	--
Ni – Si Wafer (Patterned)	0.3	0.5	50	--
			60	15/40/60
		2.0	60	--
			60	15/40/65
Ni – Si Wafer (Unpatterned)	0.3	2.0	125	--

4. FRICTION AND WEAR MECHANISMS OF HIGH PERFORMANCE ALLOYS

This section discusses the mechanisms of friction and wear of Inconel alloys.

4.1. Inconel Alloy Wear Characterization

The experimental variables for both the Inconel alloy 625 and Inconel alloy HX consisted of a range of five velocities and four normal forces. In order to evaluate the dynamic friction changes in the different alloys, the coefficient of friction of the two alloys was plotted as a function of the input mechanical work, i.e. frictional work. This can be shown in equations 7 and 8 below:

$$W = F_f \cdot d \tag{7}$$

$$F_f = N \cdot \mu \tag{8}$$

where:

W is the friction work [N•m];

F_f is the friction force [N];

d is the sliding distance [m];

N is the normal force [N];

μ is the coefficient of friction.

Since

$$N = P_c \cdot A_c \tag{9}$$

where:

P_c is the Hertzian contact pressure [N/m^2];

A_c is the Hertzian contact area [m^2].

and

$$d = V_{avg} \cdot t \qquad (10)$$

where:

V_{avg} is the average sliding velocity [m/s];

t is the sliding time [s].

Then

$$W = P_c \cdot A_c \cdot \mu \cdot V_{avg} \cdot t \qquad (11)$$

The coefficient of friction indicates the material response to contact rubbing. It is constant when surface conditions remain unchanged. Since the idealized values for Hertzian contact pressure, contact area, and velocity are used here, equation 11 can be modified to be:

$$W \propto P_c \cdot A_c \cdot V_{avg} \cdot t \cdot \mu \qquad (12)$$

It is important to note that during testing, the contact pressure and contact area will change as the pin and disk materials wear. For this study, the initial (maximum) Hertzian contact pressure was used to represent maximum input work. The variation of the coefficient of friction (μ) with the frictional work in the two Inconel alloys will be discussed individually in the following.

4.2. Friction and Wear of Inconel Alloy HX

The average coefficient of friction (μ) is plotted as a function of the frictional work for Inconel HX and is shown in figure 11. The specific wear rate (k) is also plotted as a function of friction work and is shown in figure 12. Three observations can immediately be made. The first is that there seems to be a trend for the Inconel HX to show a slightly larger coefficient of friction as the frictional work increases. This is interesting in that, as previously stated, the coefficient of friction is the materials response to the rubbing pair. The coefficient of friction represents the surface conditions at the moment when recorded, while the frictional work is the total energy introduced throughout the entire rubbing process. These results clearly indicate a close linkage between the momentary friction and the total work introduced through the test. The second observation is that at lower frictional work, the specific wear rate is the lowest; this is shown as region (1). The third observation is that as higher levels of friction work is done to the Inconel HX sample; the wear rate shows a trend to diverge, with both high and low wear rates. We notice this effect in region (2), as additional frictional work is done to the system, the tribo-behavior of the Inconel moves from regime (1) into (2). Such a clear change in the wear rate with frictional work would suggest a change in the wear mechanism of the material. Additionally, the divergence in specific wear rate may be indicative of the nature in which the surface wears. Additionally, it is known that the Inconel HX alloy has a tendency to oxide more so than the 625 alloy. Indeed, we have seen the indication of oxidation from SEM images obtained from the wear track of the Inconel HX. More details will be provided later. The higher wear rates may be caused by pure mechanical wear, while the lower wear rates indicative wear from tribo-oxidation.

Our results indicate that the effects of friction on material surfaces are accumulative through work, and not the momentary transformation of a surface under a particular certain stress. To gain a better understanding of the relationship between friction and wear, the morphologies of wear scars in each regime were studied under an optical microscope and a scanning electron microscope (SEM).

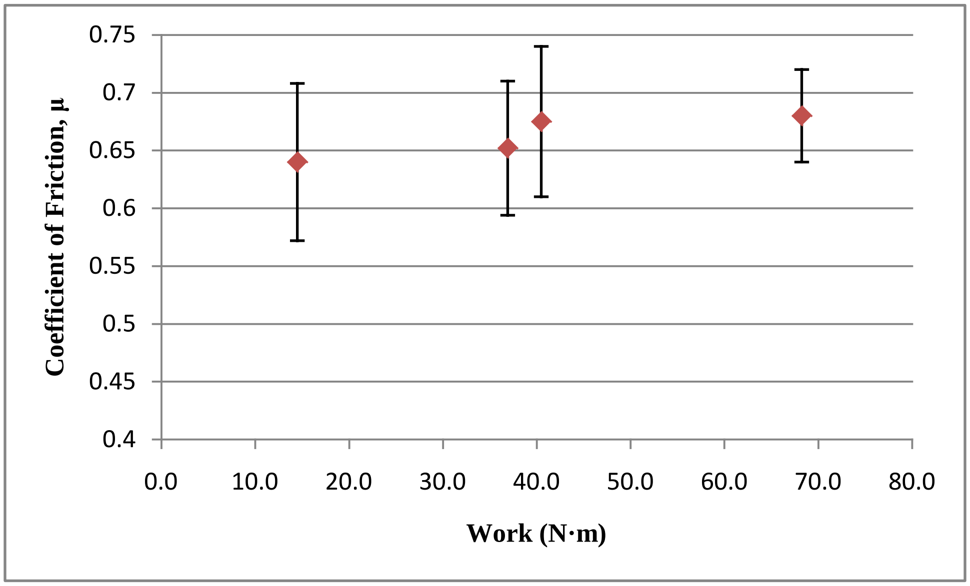

Figure 11 Coefficient of friction vs. friction work in Inconel alloy HX.

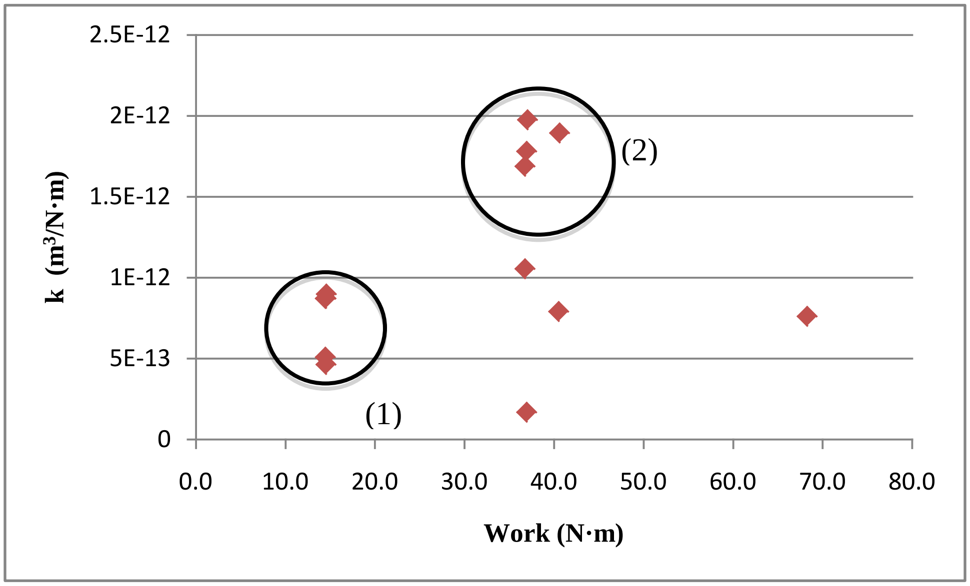

Figure 12 Specific wear rate vs. friction work in Inconel alloy HX.

4.2.1. **Low Friction - Low Wear Regime (1)**

A representative example of the morphology seen in the wear scars of regime (1) can be seen in figure 13.

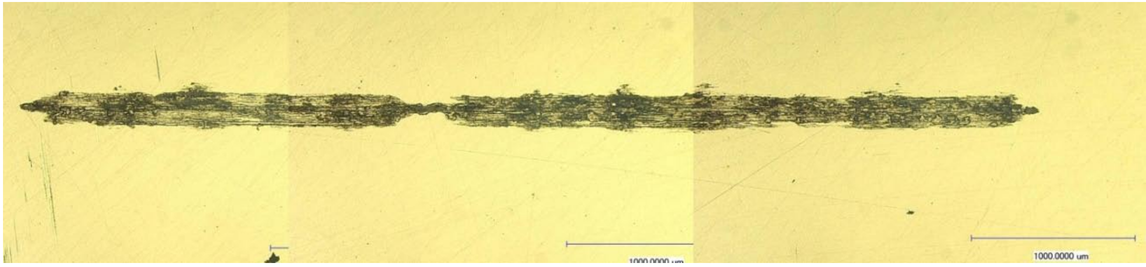

Figure 13 Optical microscope image of Inconel alloy HX wear track from friction energy regime [1]. 100X magnification.

There are three types of wear modes that can be seen in figure 13; long and uniform grooves; large single particle wear debris that appears to have been largely plastically deformed and “smeared” in the wear track; as well as large dark layered areas that look to be made of an aggregation of smaller wear debris. Figure 14 shows the wear track at a higher magnification, the three wear morphologies are highlighted.

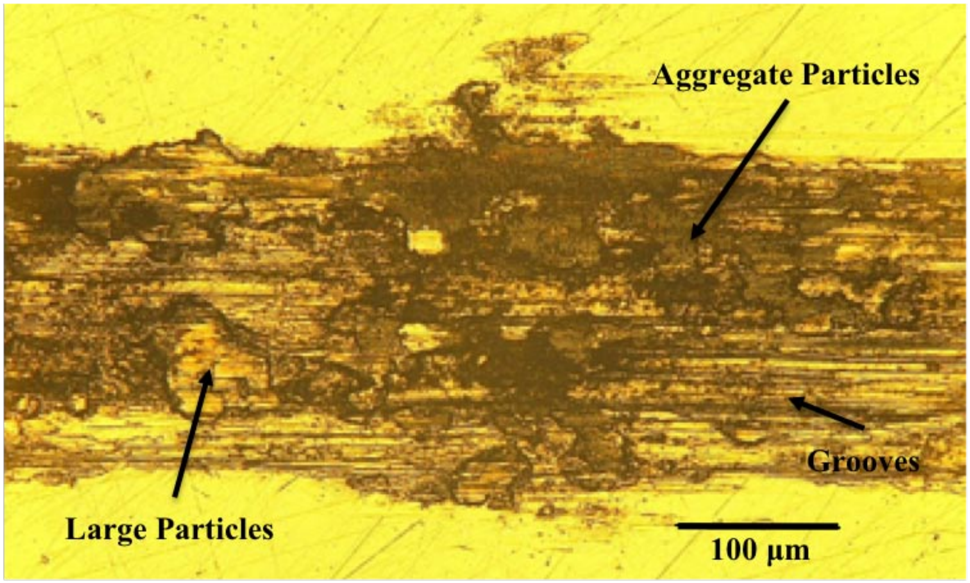

Figure 14 Optical microscope image of multiple wear morphologies in Inconel alloy HX wear track. 500X magnification.

The grooves are characteristic of abrasive wear morphology. This type of wear is to be expected in the experiment. As previously stated, the pin used in the experiment was a 440C stainless steel ball, significantly harder than the Inconel HX disk. Large asperities from the pin would essentially cut large grooves in the Inconel as the pin is passed over the counter surface. More likely, wear debris generated from the pin would act as hardened grits in the Inconel HX disk. The action imposed on these grits from the reciprocating pin would cause them to be pushed though the Inconel HX substrate, generating ploughed regions through third body abrasive wear.

The large debris that has undergone server plastic deformation and shear is characteristic of adhesive type wear. It has been shown by Buckley that nickel has one of the largest adhesive forces with iron as well as iron solubility than most metals[14]. Even low levels of friction work, would cause the Nickel Inconel disk and 440C stainless steel pin to adhere (either through friction stirring or forming a solid solution) and provide a mechanism to transfer large adhesive Inconel particles throughout the wear track. Inconel HX also has a large percentage of iron in the composition, again promoting adhesive type wear. Typical adhesive wear morphology can be seen in figure 15, a high magnification (1,300X) SEM image taken in the same area of the wear track. Note the large and highly plastically deformed layers, indicative of adhesive wear[12]. It should also be noted that Inconel HX alloy is an extremely ductile material at room temperature with an elongation to failure of 45%[34]. Since adhesion is more typical in ductile materials, significant amounts of adhesive wear can be expected in the Inconel HX alloy. This factor was also apparent during testing, as the higher normal loads were not successfully tested on the counter-surface due to significant adhesion to the pin.

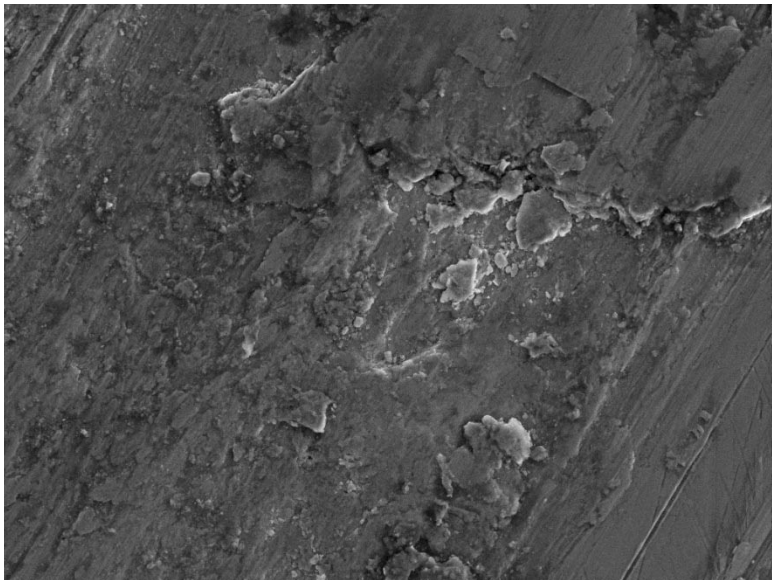

Figure 15 Optical microscope image of multiple wear morphologies in Inconel alloy HX wear track. 500X magnification.

The third type of wear morphology seen in regime (1), consists of a layer of aggregated wear debris. Figure 16 is a high magnification optical microscopic picture of this type morphology.

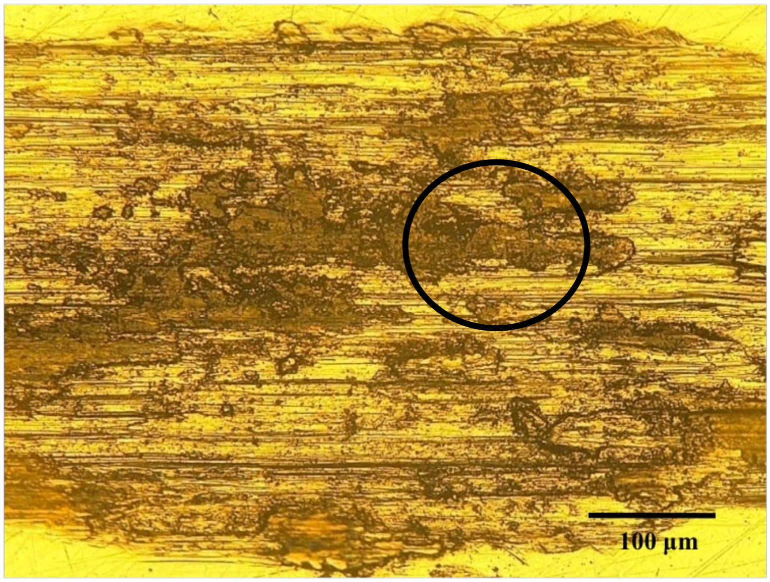

Figure 16 .Optical microscope image of aggregate particle wear morphology in Inconel alloy HX wear track. 500X magnification.

Figure 17 is a SEM image of the same morphology at a higher magnification. It has been highlighted in Figure 16 for coherence in this thesis. The transition from optical microscope to the SEM was for the ability to obtain non-parallax images at larger magnifications.

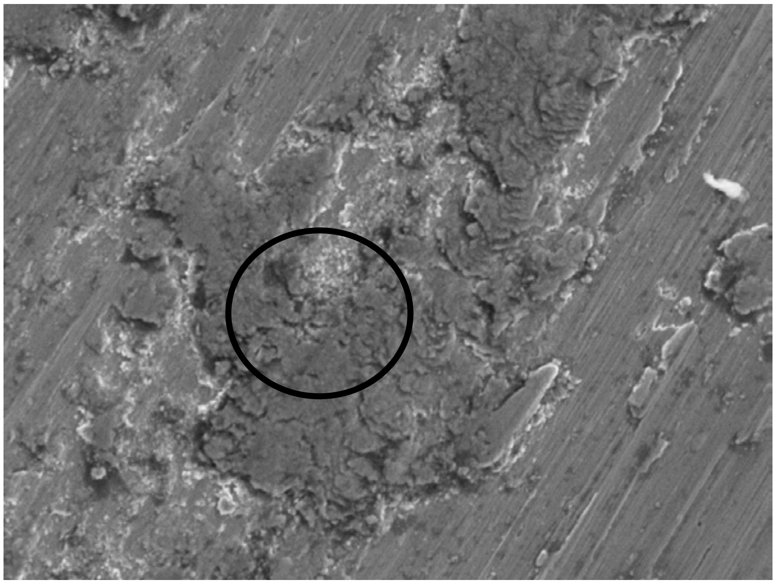

Figure 17 SEM image of aggregate particle wear morphology as seen in figure 7. 1000X magnification at 15,000 eV.

It is interesting to note the layered “wave” morphology formed by the wear debris. This morphology shows a structure of debris that has been formed in response to multiple-cycles of the reciprocating pin; it is heavily deformed in the friction direction. Additionally, the morphology shows a layered structure higher than the rest of the sample. This indicates that it has been built up during the process of testing. This evidence supports the assumption of an aggregated layer of wear debris.

The morphology of interest in Figure 17 has been hi-lighted and magnified in Figure 18.

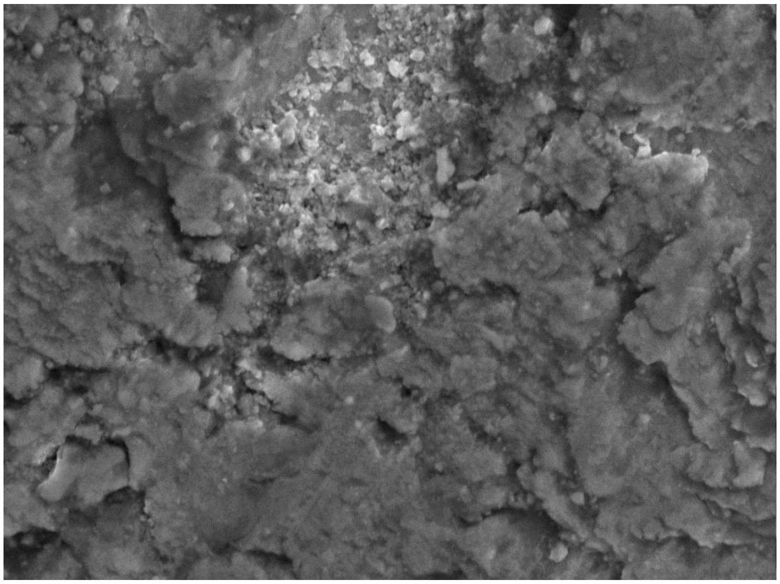

Figure 18 SEM image of aggregate particle wear morphology hi-lighted
in Figure 8. 4000X magnification at 15,000 eV.

At a high magnification (4,000X), the large aggregation of wear debris appears to actually be a collection of small particles that have been plastically deformed and smeared together in that track by the motion of the reciprocating pin. Additionally, very small individual particles can be seen by a large change in the contrast of the SEM image. Despite the edge effects evident in some of the debris layers, the bright color indicates the oxidative metal debris as compared to the darker particles. The oxide is apparently introduced during sliding. Stachowiak and Batchelor have noted that oxidative wear has been observed at low sliding speeds (lower than 1m/s)[5]. The oxide film is typically present natively on the surface of the material and then due to the slow sliding speeds, only minimally generated on large individual asperities of the pin and disk. The morphology would suggest that brittle native oxides and oxidized metallic wear particles broken during the reciprocation and then compacted in the wear track to form oxide 'islands' on the worn surface [45]. The formation of these oxide islands is alike to the aggregate morphology seen from the optical micrographs. The evidence of oxidized particles seen in the SEM images in combination of optical microscope images is convincing evidence of the competing wear modes of adhesion and abrasive wear dominated by the build-up of these oxide islands.

4.2.2. **High Friction Work – High Wear Regime (2)**

A representative image of the wear morphology seen in regime (2) can be seen in figure 19.

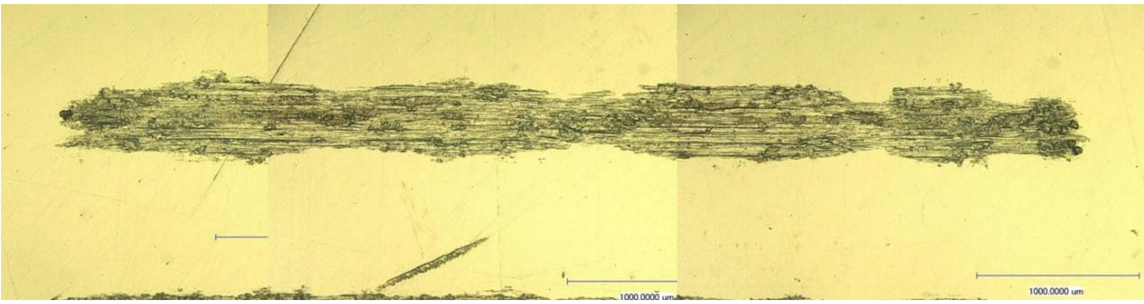

Figure 19 Optical microscope image of Inconel alloy HX wear track from frictional energy regime (2). 100X magnification.

When higher levels of friction energy is input into the system, the Inconel displays the abrasion and adhesion type morphology but does not display the large areas of oxide island morphology. A higher magnification of the wear track is shown in Figure 20.

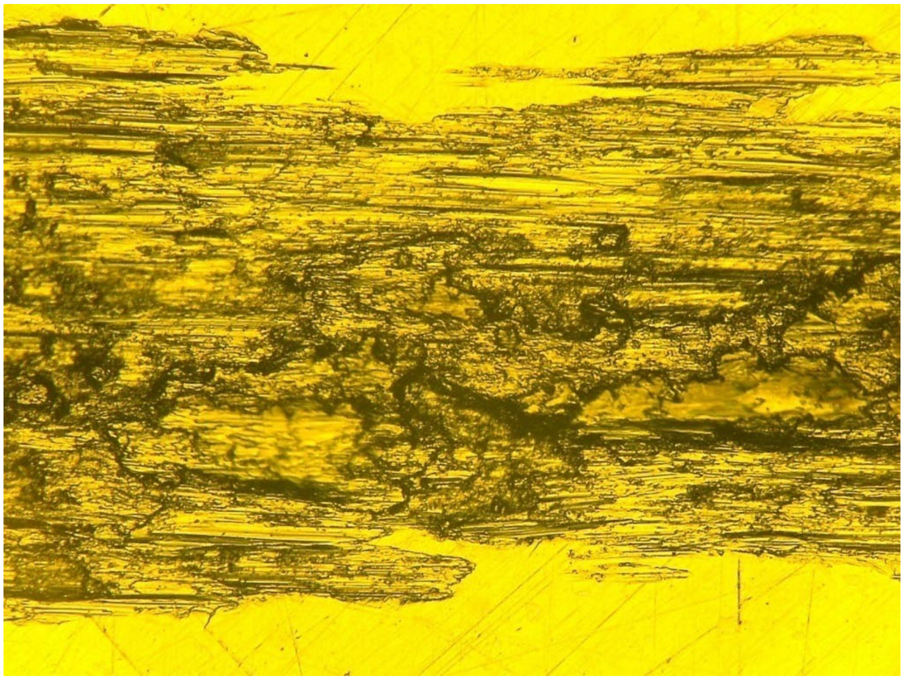

Figure 20 Optical microscope image of Inconel alloy HX wear track from frictional energy regime (2). 500X magnification.

The characteristic ploughing morphology of abrasion is evident in the disk, and can specifically be seen in the top part of the wear track. The large, highly deformed particles on the wear surface, characteristic of adhesive wear, are also evident in the micrograph. Interestingly, the large, dark, “oxide islands” are not evident in the wear morphology of Inconel HX at higher friction energy levels. At this point, the wear modes in Inconel HX are dominated by abrasive type wear with elements of adhesion.

4.3. Friction and Wear in Inconel 625

The average coefficient of friction is plotted as a function of friction work for in Inconel 625 in figure 21. Both Inconel 625 and HX showed similar ranges of coefficient of friction, however, the Inconel 625 shows a more distinct trend of increasing average coefficient of friction with frictional work than that of Inconel HX. This trend is to be somewhat expected as Inconel 625 is a work hardenable alloy[33]. As the surface Inconel material in the wear track is hardened under higher levels of friction work, the contact and sliding conditions between pin and countersurface will change, thus being reflected by a change in the average coefficient of friction.

It is also interesting to note the trend in the standard deviation of the Inconel 625 coefficient of friction with increased work. It is apparent from figure 21 that as the work level increases; deviation in the average coefficient of friction is reduced. This could be indicative of a change in wear mechanism from multi modal wear to single mode wear, and/or a process induced change in the material, leading to more consistent and predictable sliding conditions between pin and countersurface.

The specific wear rate shown in figure 22, displays a clear increasing trend in wear rate as friction work is increased. Such a sharp increase in wear rate is typically indicative of abrasive wear. Furthermore, contact conditions involving abrasion have long been recognized as being some of the most significant in terms of the amount of material loss[46]. The trend towards high wear rate could also be a function of the work hardening of the Inconel 625, hardened wear debris from the Inconel surface would cause third body abrasive wear. Overall, in comparison with the HX alloy, the wear of the 625 alloy shows a shows a slightly lower wear rate as a function of the frictional work. This is most likely dues to a lack of oxidative wear.

We examined the wear track morphologies in the three distinctive regions of friction work to determine the nature of the wear and determine any change in wear mode. The regions compared are circled in figure 22.

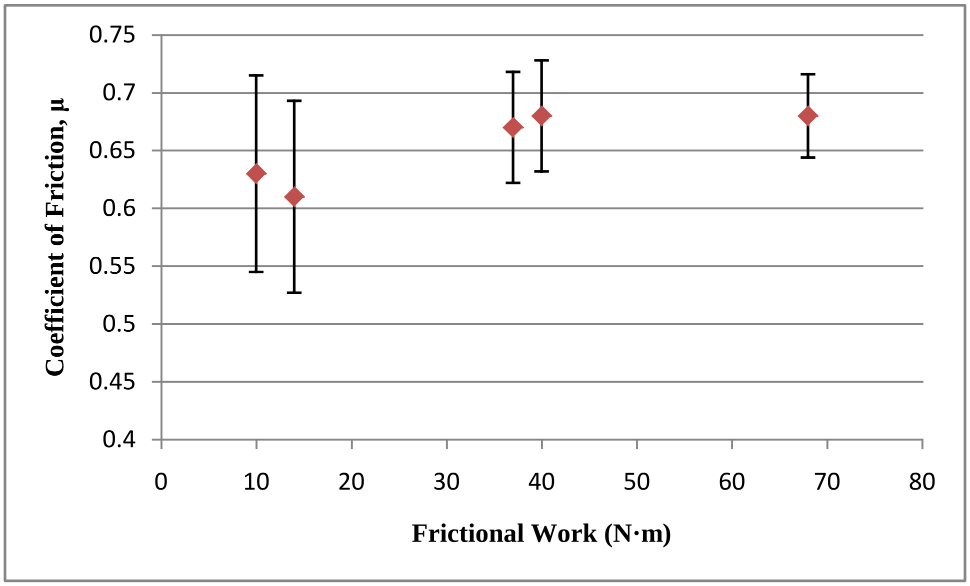

Figure 21 Coefficients of friction vs. friction work in Inconel alloy 625.

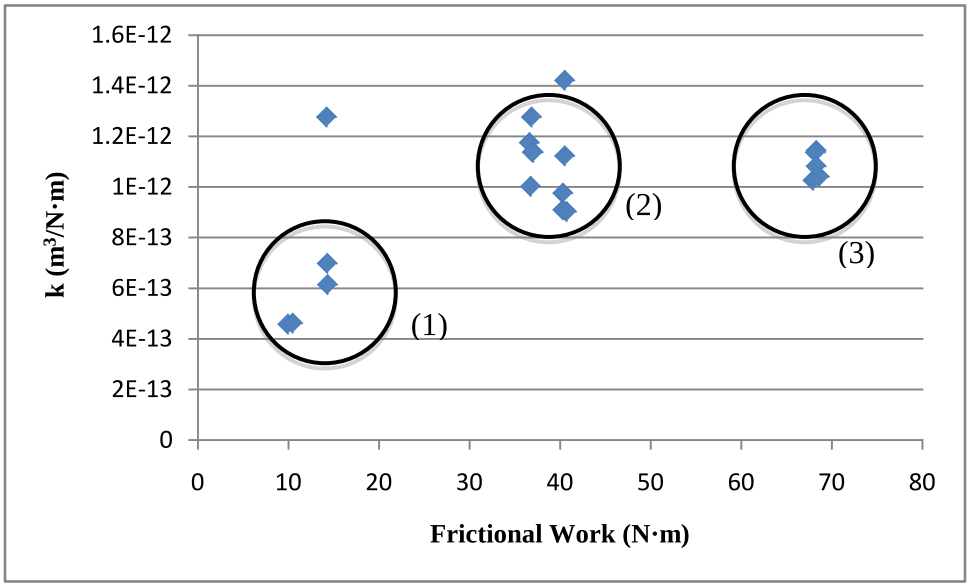

Figure 22 Specific wear rate vs. frictional work in Inconel alloy 625.

4.3.1. **Low Friction Work – Low Wear Regime (1)**

In the lower frictional energy and wear region, the Inconel 625 shows a trend towards two different wear modes. In the wear tracks that showed low values of specific wear rate, the wear modes are similar to that of the Inconel HX alloy, showing characteristics of both adhesive and abrasive wear. It is interesting to note that the oxidation “islands” are nearly nonexistent. A representative wear track in region (1) is shown in figure 23 below. In the figure, the darker areas are the adhered debris and lighter ones are abrasive wear.

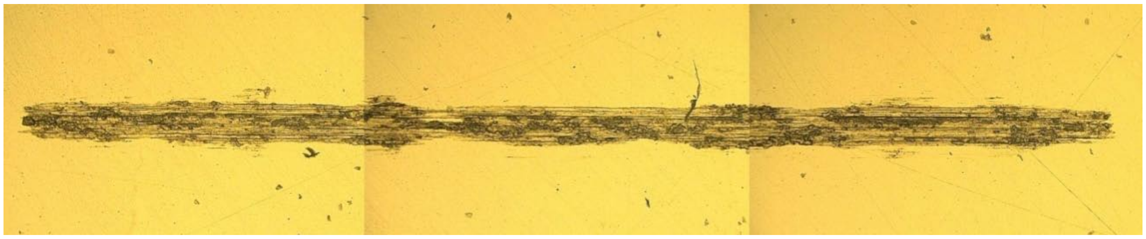

Figure 23 Optical microscope image of Inconel alloy 625 wear track
from the low energy – low wear region (1). 100X magnification.

At a higher magnification (500X), as seen in Figure 24, it is easier to distinguish the different wear modes of the Inconel 625. At lower frictional energy, the wear of the material is dominated by abrasive and adhesive wear. No morphology characteristic of the oxide “islands” can be seen.

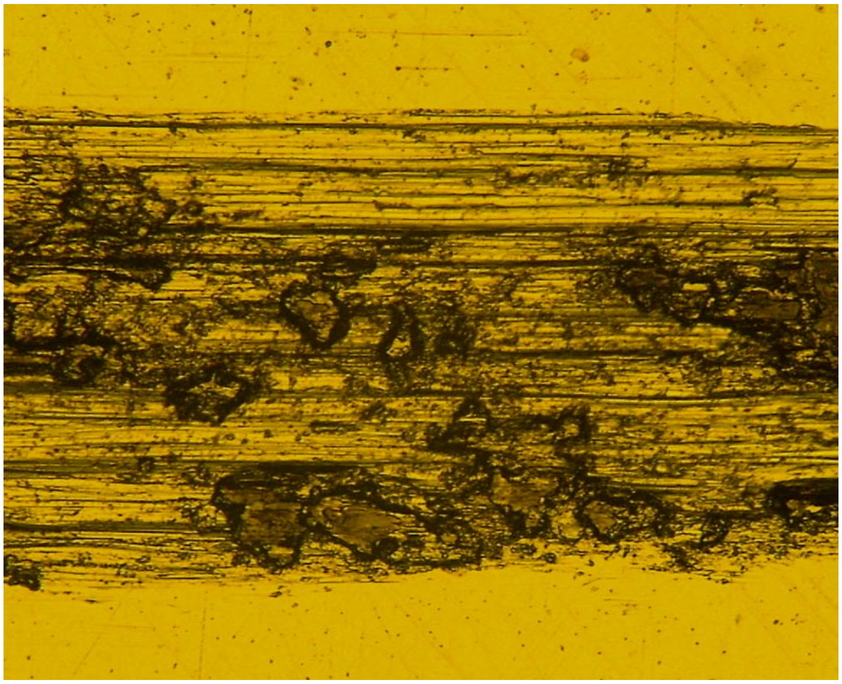

Figure 24 Optical microscope image of Inconel alloy 625 wear track from the low energy - low wear region (1). 500X magnification.

4.3.2. **Moderate Friction Work – High Wear Regime (2)**

In the moderate energy and high wear region (2), the wear mode is characteristic of abrasive type wear. Figure 25 is a representative wear track from the region. The typical grooves genereated due to abrasive wear are clearly visable. Interestingly, particulate debris indicative of adhesive mode wear cannot be see in the wear track, this would indicate that abrasive wear is dominate.

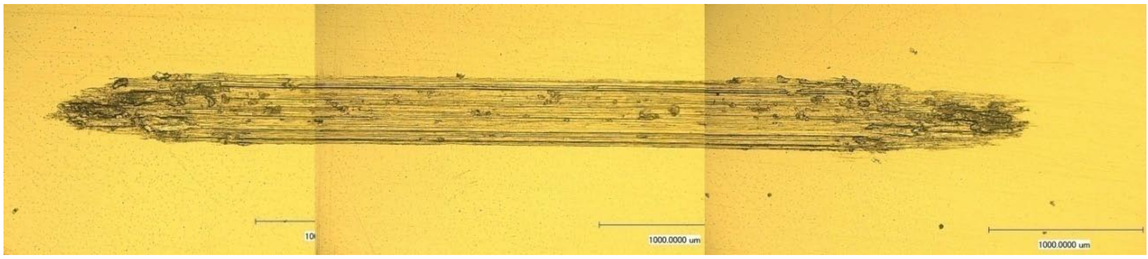

Figure 25 Optical microscope image of Inconel alloy 625 wear track from the moderate energy - high wear region (2). 100X magnification.

A more significant observation is the transition in wear modes of the material at a higher frictional energy input.

4.3.3. **High Energy - High Wear Regime (3)**

At higher frictional energy and higher wear levels (3), the wear in Inconel 625 was dominated by abrasive type wear, similar to the previous example. Evidence of this can be seen in figure 26, by the uniform ploughing and the lack of adhesive debris in the wear track. As mentioned earlier, the wear modes are dependent on the contact pressure or sliding speed. These results further confirmed that the abrasive wear promotes more wear while adhesion otherwise.

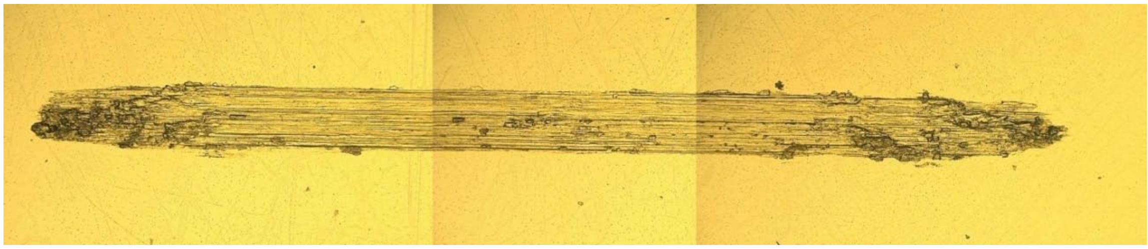

Figure 26 Optical microscope image of Inconel alloy 625 wear track
from the high energy - high wear region (3). 100X magnification.

4.4. Ending Remarks

This section discussed the friction and wear mechanisms of two high performance materials. The readily available high strength nickel-based alloys were studied on a pin-on-disk tribometer under a range of sliding speeds and loads. The tribological performances of the two Inconel alloys were compared over a range of frictional energy and wear modes. The results showed interesting friction and wear behaviors and mixed modes of wear mechanisms were revealed.

It was observed that the frictional work plays an important role in tribotesting. To date, there are no test mechanisms to studying such a dynamic nature of materials. In the following two sections, further study will be discussed in terms micro-to-macroscopic friction and the dynamic tribotesting.

5. SPATIAL EVOLUTION AND IN SITU OBSERVATION OF FRICTION – A MICROTRIBOLOGICAL APPROACH

This section discusses a method of monitoring friction and the in situ observation of friction and wear of a patterned surface structure.

5.1. Layered Metal Composite

The properties and structures of the layered metallic composite were described in Section 3. This sample was studied in this research for two reasons. The first was that samples with micro geometry had never been tested utilizing this technique before. Since various metal sheets were available, a simple composite sample constituted of materials with distinctly different tribological behaviors was created. The second reason for the test of the layered metal sample is to study the relationship between average coefficient of friction of a composite material and the individual friction behaviors of the composite's constituents. The data presented below is representative of all the friction tests done on the sample.

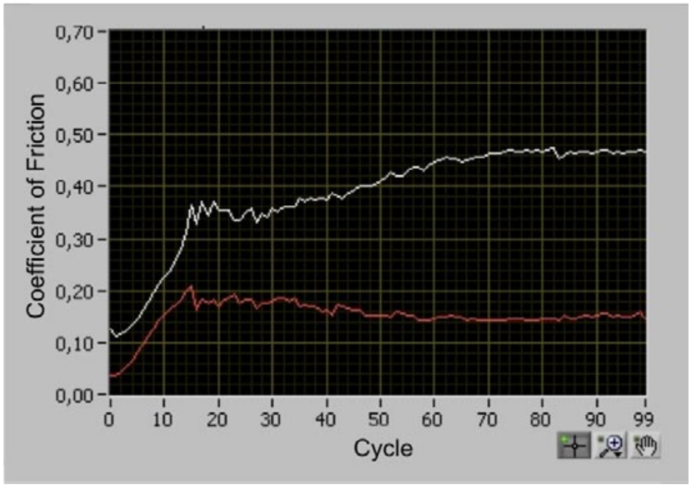

Figure 27 Average coefficient of friction versus wear cycle (white) for metal composite sample. RMS μ versus wear cycle (red).

Figure 27 shows the average coefficient of friction (COF) (upper) and root mean square (RMS) coefficient of friction (lower) versus wear cycle. The coefficient of fiction is plotted on the y – axis with respect to the friction cycle, plotted on the x – axis. The average COF is the numerical mean of all 512 samples taken in a single reciprocation of the pin. The root mean square coefficient of friction is the statistical measure of the magnitude variance of the samples. The RMS friction trend is plotted in red and shows little variance in the trend of the average COF. This indicates that little error in the average coefficient of friction trend.

From the start of the test we can see that the coefficient of friction rises rapidly and continues to fluctuate until reaching a steady value after about wear cycle 30. This is a common phenomenon in tribology contact called *run-in*. The run-in is a result of the tribosystem adjusting to reach steady state conditions between contact pressure, surface roughness, and the interfacial layer, and establishment of an effective lubricating film in the wear track[47].

After run-in, the average coefficient of friction continues to increase slightly in magnitude until wear cycle 60 in which it reaches a true stead-state. This type of behavior is similar to what is seen in unlubricated metal-on-metal contact[48]. It’s interesting to note that even though the sample is made from constituents of four different materials (phases) with different tribological behaviors, the friction behavior of the sample is similar to a single homogeneous metal. The root mean square (RMS) COF is the statistical measure of the magnitude variance of the samples. The RMS friction trend is plotted in red and shows little variance in the trend of the average COF.

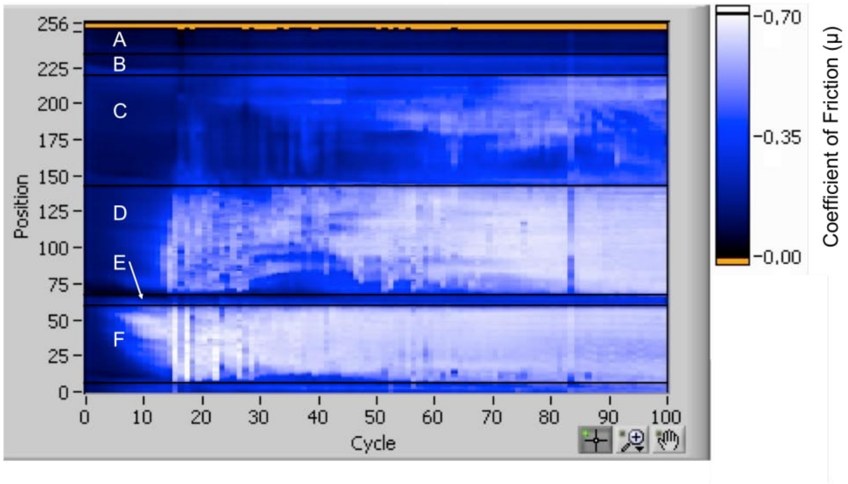

Figure 28 Friction Map for metal composite. Layer Structure labeled as follows: A. Phenolic. B. Phenolic. C. Stainless Steel. D. Brass. E. Phenolic Layer. F. Copper.

The coefficient of friction map for the metallic layer sample is shown in figure 28. The position of each friction sample in the wear track is shown on the y – axis divided into 512 elements, the vertical resolution of each element being approximately 7μm. The friction cycle is plotted on the x – axis. The friction key is shown in the scale bar on the right for reference. The low friction elements are colored closer to black whereas the higher friction elements are colored closer to white. The technique is able to distinguish changes in coefficient of friction from subsequent friction cycles as the pin passes over the layered constituents of the sample.

Since each material exhibits different frictional behavior in contact with the pin, very distinct friction "zones" are seen. These zones are labeled A through F in the figure above. The resolution of the friction measurements is high enough to determine the interface between the relatively small amount of polymer between the brass and copper layers, show by zone “E” in figure 28. The phenolic polymer layer is only 20 μm in thickness, however, the difference in the coefficients of friction between it and the two surrounding metals are great enough to clearly show the interface.

It is also interesting to observe that the evolution of friction in each material is clearly captured by the friction map. For instance, in the stainless steel, the friction increased slowly over many friction cycles while the copper presented a large initial coefficient of friction that slowly became stable by the end of the test.

One important observation that should be made is that high friction stick-slip phenomenon was not seen in the test until the last twenty cycles. The phenomenon was indicated by a repeating oscillation between low and high values of coefficient friction in the lateral direction, most prominently seen in Cu in zone “F”. The stick-slip often becomes prominent in low stiffness tribometer systems, when the pin-countersurface contact and friction forces are high. Testing was stopped after significant stick-slip was observed as unrepresentative wear and noise were generated.

5.2. Ni – Si Wafer

Once the testing technique was successfully demonstrated by the layered metal composite, the micro Ni – Si wafer was tested. As described previously in the testing matrix, multiple tests at various loads and speeds were run on the Ni-Si wafer. Post-testing analysis of the Ni – Si sample data has shown no significant difference in friction or in electrical contact resistance behavior between loads or speeds. The data presented below is the best data available, representative of all testing conditions.

Figure 29 shows change in the COF of the experimental wafer during tribological testing.

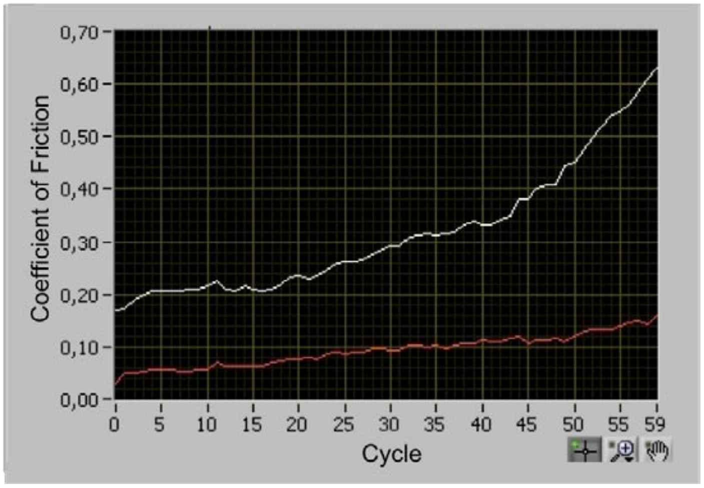

Figure 29 Average (white) and root mean square (red) coefficient of friction (COF) per wear cycle for experimental wafer during testing.

The values for the average coefficient of friction (COF) (upper) and root mean square coefficient of friction (RMS) (lower) are plotted on the y – axis with respect to the friction cycle, plotted on the x – axis. The average COF is the numerical mean of all 512 samples taken in a single reciprocation of the pin. The root mean square (RMS) coefficient of friction is the statistical measure of the magnitude variance of the samples. The RMS friction trend is plotted in red and shows little variance in the trend of the average COF, indicating little error in the measurement.

It is clear from figure 29 that the average coefficient of friction goes through three distinctive trends. From the start of the test to cycle 15, the COF remains low and stable. From cycle 15 to cycle 40 the COF experiences a small increase with subsequent friction cycles, most likely due to changing surface roughness effects. The third trend shows the COF rate increases again at approximately cycle 45 and continues increasing until the end of the test. The numerical friction values are consistent to what has been shown for tribological experiments on silicon done previously by Venkatesan and Bushan [49], however, the friction trend is not. This is most likely due to the special textured surface that we have. Figure 30 shows the friction map generated during testing.

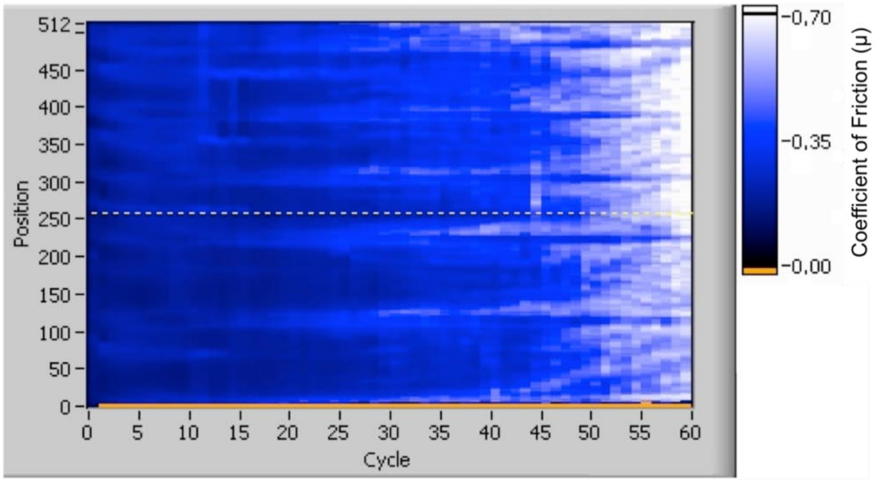

Figure 30 COF mapping.

The position of each friction sample in the wear track is shown on the y – axis divided into 512 elements, the vertical resolution of each element being approximately 7μm. The friction cycle is plotted on the x – axis. The friction key is shown in the scale bar on the right. The low friction elements are colored closer to black whereas the higher friction elements are colored closer to white. The technique is able to distinguish changes in COF as the pin passes over the individual nickel strips, as shown by the striation of white horizontal lines most distinctive in the first friction cycles. As correlated by the average COF plot shown earlier, a visible change in the friction trend begins around cycle 15. Higher friction zones begin to develop at the interface between the Si substrate and Ni strips. Between cycles 15 and 40, friction continues to be highest at the interface but is no longer localized there, spreading across the sample. Soon after cycle 45 high friction dominates the entire wear track, and at this point the sample wear track is considered destroyed.

Figure 31 shows the average and RMS change in the electrical contact resistance (ECR) of the experimental wafer during testing.

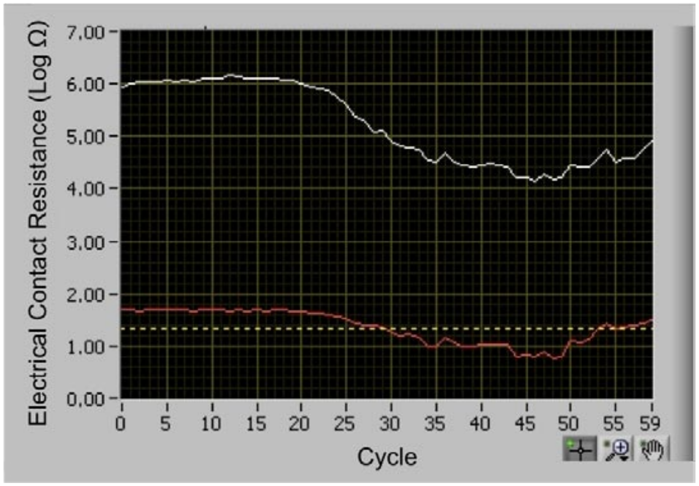

Figure 31 Average (white) and root mean square (red) electrical contact resistance (ECR) per wear cycle for experimental wafer during testing.

The values for the average (upper) and RMS (lower) ECR are plotted in Ohms (Ω) on the y – axis on a log scale with respect to the friction cycle, plotted on the x – axis. It is clear from figure 31, the average ECR also demonstrates three distinctive trends in a similar fashion to the average COF but slightly delayed in occurrence. In the first 20 cycles, the ECR remains stable. At cycle 20 the ECR begins to drop quickly from 10^6 Ω to 10^5 Ω, an order of magnitude in approximately 10 cycles. This average ECR continues to decrease until cycle 45 at which point it reaches the lowest resistance value during the test, 10^4 Ω. The final period of the test, from cycle 45 until finish, the resistance begins to rise, most likely due to damage in the wear track. The RMS again indicates little significant fluctuation in the average ERC trend.

Figure 32 Shows the electrical contact resistance map generated during testing.

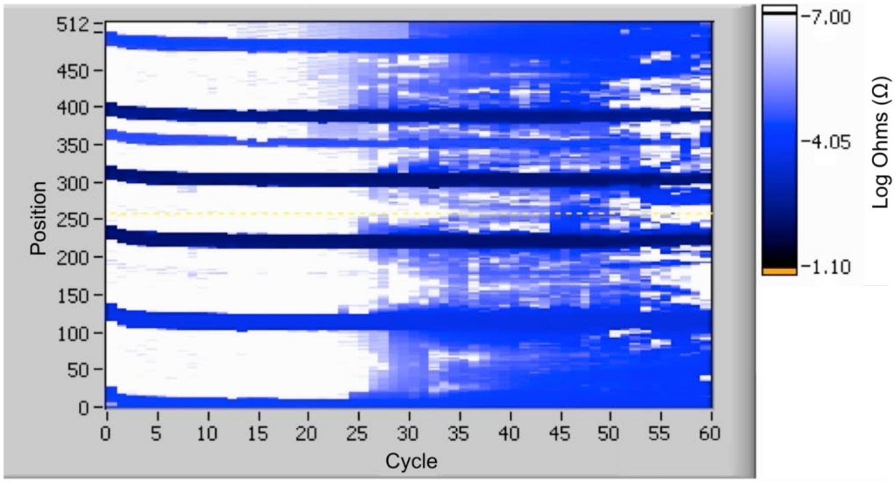

Figure 32 ECR Map.

The position of each element in the wear track is shown on the y – axis. Spatial resolution of each element is equal in scale to the friction map. The friction cycle is plotted on the x – axis. The resistance key is shown in the scale bar on the right. The low resistance elements are colored closer to black while the high resistance elements are colored closer to white. The low resistance nickel tracks can easily be distinguished from the high resistance silicon substrate. It is noted that not all nickel tracks are “visible” in the ECR map. Various tracks had been physically severed previous to the experiment and were not able to conduct electricity. These tracks do show up in the friction mapping but do not show up in the ECR mapping. The evolution of the average ECR throughout the test is highlighted with more detail by the ECR map. From start to approximately 20 friction cycles, little change is visible in the ECR. Soon after cycle 20, a low resistance gradient in the ECR of the wafer is clearly shown to develop again seemingly at the nickel and silicon interfaces. As the test proceeds, the low resistance gradient quickly spreads across the insulative silicon layers becoming nearly homogeneous in throughout the entire wear track until cycle 50. From cycle 50 to the end of the test, high resistance areas begin to appear again. This trend in ECR change is consistent with the trend in friction change of not slightly offset in friction cycle. This would seem to indicate that the surface properties in the wear track are being modified as a result of the frictional change. To investigate the effects of friction cycles on the wear of the sample, a multi-sequential test was done to provide three distinctive and measurable areas of wear. The change in amplitude was configured such that the last-cycle wear in each region captures any detectable wear morphology leading to the unique electrical contact resistance behavior. The muti-sequential wear map is shown in figure 33.

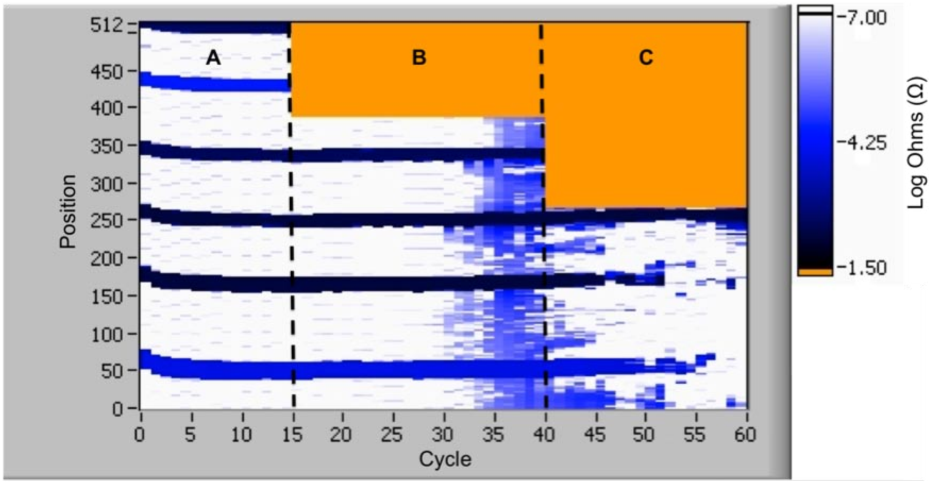

Figure 33 Multi-Sequential ECR map.

In similarity to the ECR map shown in figure 32, the position of each element in the wear track is shown on the y – axis. The x – axis is again showing the friction cycle. Additionally, there are two zones in which resistance data is not displayed. These zones are ones in which the amplitude of the friction cycle was changed and data is no longer sampled. This effectively defines the three distinct wear zones, which have undergone progressively longer friction cycles: The light wear zone, labeled as “A”, moderate wear zone “B”, and severe wear zone “C”.

Figure 34 shows an optical micrograph taken of the wear track after the multi-sequential friction test.

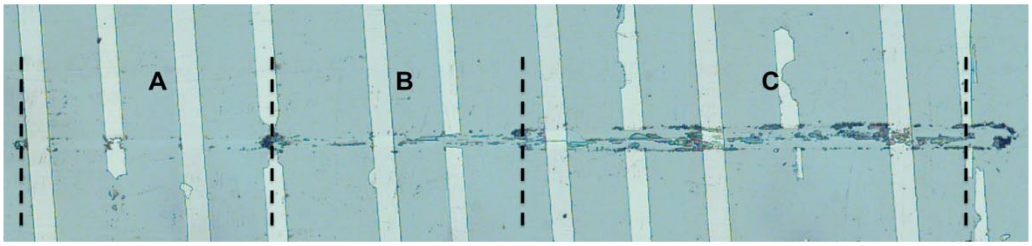

Figure 34 Optical micrograph of multi-sequential wear track.

The light, moderate, and severe wear zones from the test have been labeled in the figure using the same format corresponding to ECR map in figure 33. In zone “A” we see evidence of wear as indicated by a slight color difference in the Si substrate and minimal removal of material from the nickel tracks. In zone “B” we see a slightly wider wear track in the substrate containing visible nickel debris. In one case, the friction has been significant enough to have worn through the width of a nickel strip. In zone “C”, we see the widest wear track and substantial amounts of nickel debris scatter through the track. The wear track showed little evidence of wear in the silicon substrate, even at high optical magnifications. There is evidence of wear by the existence of nickel debris, but it does not seem substantial or uniform enough to cause high levels friction, or lower levels of contact resistance. A higher resolution method for investigating wear on the silicon surface was needed.

5.2.1. **3D Wear Track Analysis**

To investigate the wear effects on the surface a Zygo NewView 600 white light interferometer was used to determine the surface profile of the silicon substrate in each wear region. The results of these measurements are shown in figures 35 to 37.

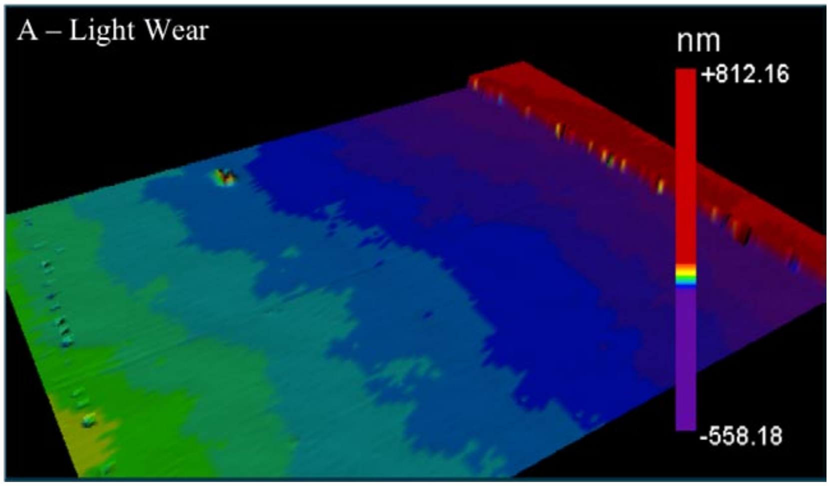

Figure 35 Three dimensional surface profile of light wear region of Ni – Si wafer sample.

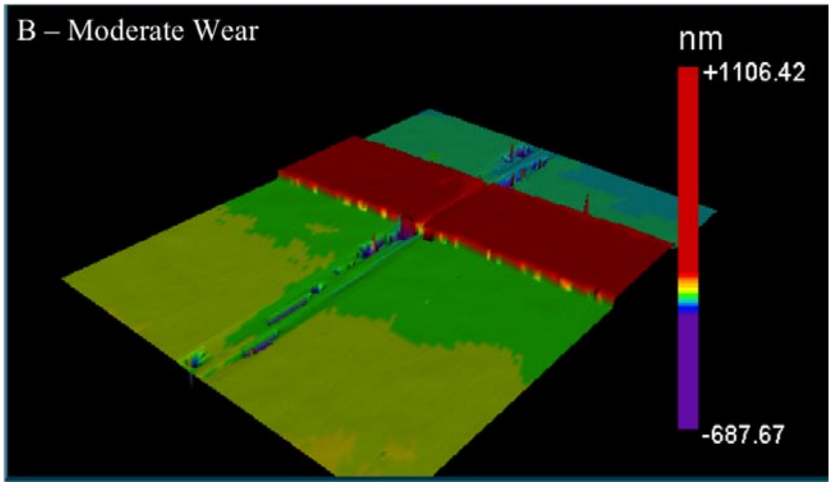

Figure 36 Three dimensional surface profile of moderate wear region of Ni – Si wafer sample.

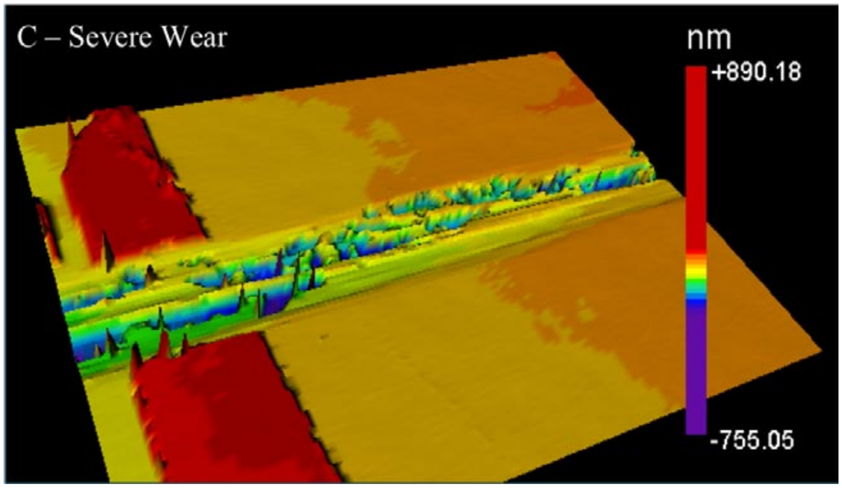

Figure 37 Three dimensional surface profile of severe wear region of Ni – Si wafer sample.

The data for the profilometer readings is shown in table 16.

Table 16 Surface roughness data for each wear zone from Zygo NewView 600p white light interferometer.

Wear Region	Average Surface Roughness of scanned area (Ra) µm	Average Surface Roughness in Wear track (Ra) µm	Average Surface Roughness in Wear track (RMS)	Average Depth of wear damage µm
A – Light	0.023	0.002	0.032	0.0015
B – Moderate	0.041	0.024	0.035	0.107
C – Severe	0.028	0.067	0.093	0.34

It is evident from both the three dimensional surface profile representations, along with the readings of average surface area in the wear track that the surface roughness of the silicon substrate increases significantly with friction cycles. Additionally, more severe wear damage is done to the substrate with each friction cycle as indicated by the increasing the depth of wear damage.

5.2.2. **XPS Wear Track Analysis**

To investigate the nature of any tribo-films that may have been formed during pin on disk testing X-ray photoelectron Spectroscopy was done to characterize elemental traces of nickel, iron, and silicon in the three different wear tracks. The surveys for each element are shown in figures 38 to 41.

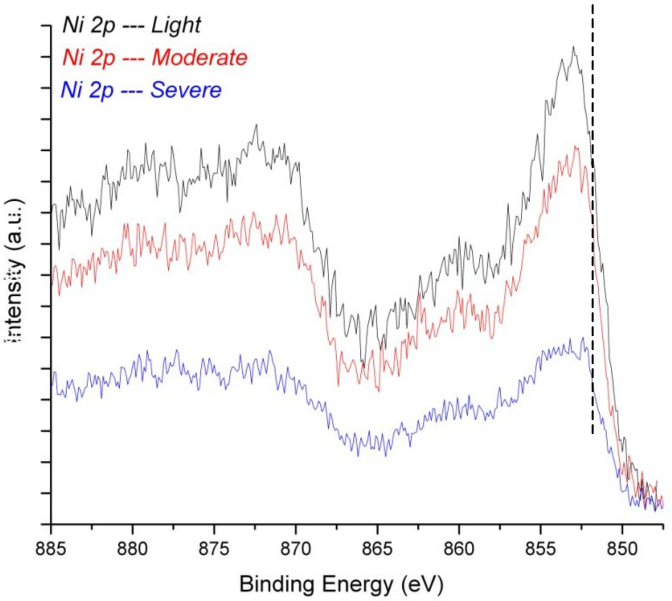

Figure 38 XPS results of binding energy survey for Nickel 2p.

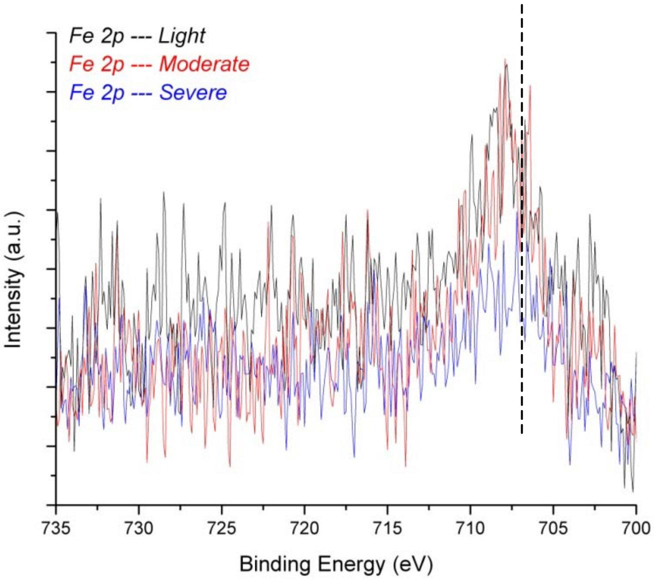

Figure 39 XPS results of binding energy survey for Iron 2p.

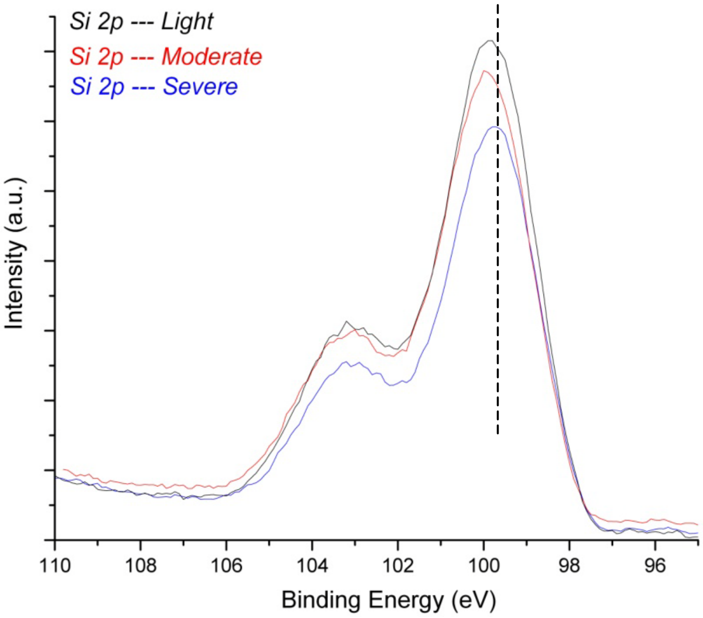

Figure 40 XPS results of binding energy survey for Silicon 2p.

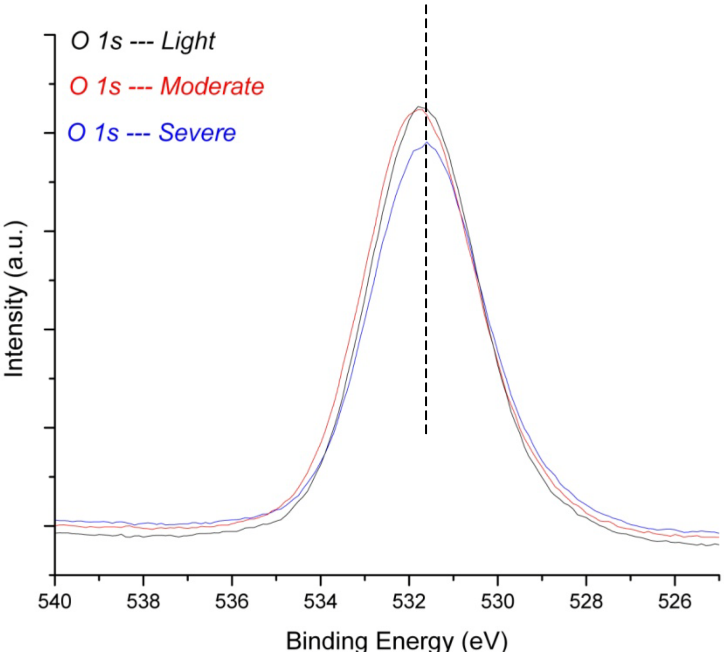

Figure 41 XPS results of binding energy survey for Silicon O1s.

The XPS analysis shows that there is a shift in binding energy of the silicon and oxygen peaks under severe wear. This is an indication that the oxidation of silicon was likely to occur during the extensive wear region. The binding energies of nickel and iron peaks on the other hand, remain unchanged. Those elements did not tribochemically react with other materials during sliding, most likely the nickel and iron were mechanically blended into the substrate.

The iron, however, showed significantly lower emission intensity between the light and severe wear regions (the exact values are not shown). This would mean that iron from the pin was transferred to the countersurface at the beginning of the experiments. After a period of extensive sliding, the transferred iron then detached from the countersurface.

The nickel, on the other hand was transferred from its original location (strip) to the silicon surface. As the friction cycles progressed, the nickel and silicon are mechanically blended into each other. The transfer of materials continues gradually till the end of the moderate wear region in which the resistivity reaches the lowest value.

As sliding continues wear damage and oxidation of the silicon becomes more dominate and the resistivity begins to increase. Results obtained from XPS, ECR, COF, and Ra are all consistent with the arguments.

5.3. Ending Remarks

This section discussed the tribological behaviors of micro textured surfaces using an in situ approach and pin-on-disk tribometer. The test conditions used were very simple; a fixed applied load under constant mechanical energy input. The process of material transfer was closely observed using the unique approach. In the next section, we will discuss a new method that is capable of dynamic tribological testing.

6. DESIGN OF A DYNAMIC TRIBOMETER

The focus of this section is on the design and application of a novel tribometer developed for dynamic friction experiments.

6.1. Concepts

As shown in previous experiments, electrical contact resistance (ECR) measurement is effective in observing the nature of the contact between two metallic surfaces. Electrical contact resistance has been used for many years to investigate the effects of friction between two conductive surfaces. A good deal of historical research in this area has focused in applications to the field of electrical engineering and not tribology. As widespread use of electrical contact switches and brushless motors were becoming prevalent, engineers like Ragnar Holm were investigating the effects of friction on contact resistance and vice versa[50].

It has been mentioned that a relationship exists between the coefficient of friction and ECR. There also exists a proportional relationship between load and ECR through the true contact area [5]. Therefore, the ability to manipulate the load during contact and observe instant feedback of the coefficient of friction and ECR could be instrumental in understanding how additional solid contact mechanics are changing in situ. As an example, figure 42 below suggests how in situ contact stress, could be experimentally studied using variable loading conditions and electrical contact resistance.

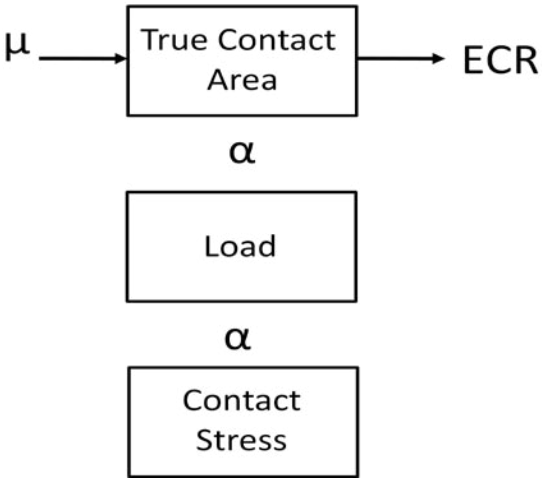

Figure 42 Example of friction study utilizing variable load and ECR.

Along with giving variable in situ measurements, the tribometer can be used to determine the dynamic response of a material to variable loading cases. Common examples of engineered systems under dynamic friction conditions include aircraft landing gear, friction brakes, etc. As a more original example, the joints in a human knee see variable loading conditions everyday as one walks to and from work. This tribometer would allow quick and cheap investigation of similar cyclical loading cases before the expense of complicated joint simulation tribology machines.

6.2. Design

To build a comprehensive, dynamic system, the variable tribometer was designed around the CSM Macro-Tribometer with the addition of an apparatus in which to vary the normal load on the pin. The CSM Macro tribometer has the advantage of the on board motor control and a high precision sensor system in which to detect the tangential force. The system also has full data accusation and analysis software. The CSM Macro-Tribometer as received from the factory is shown in figure 43.

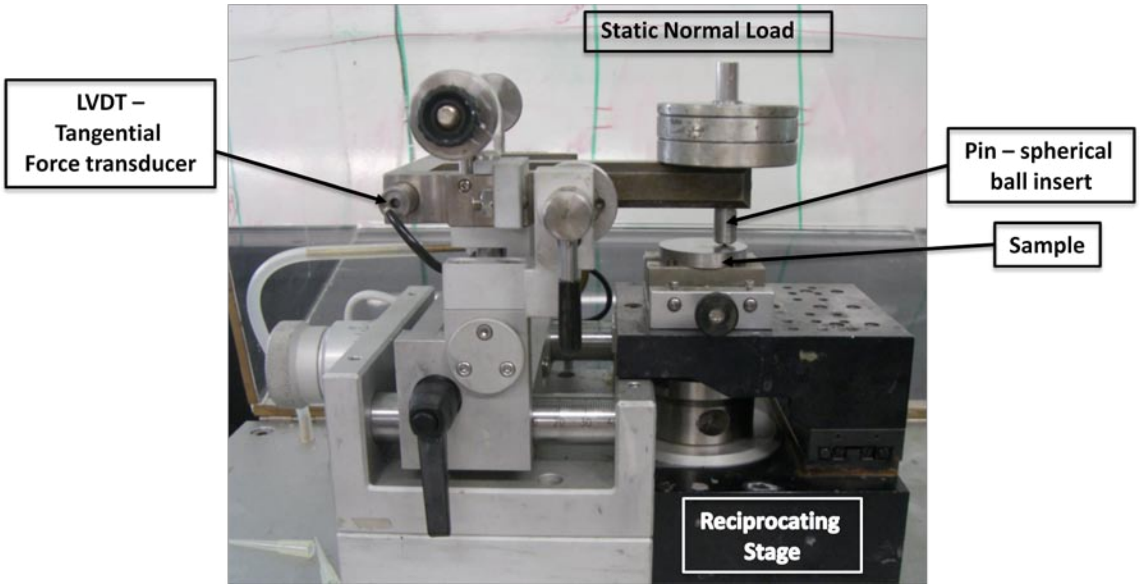

Figure 43.CSM Macro Tribometer.

As shown in figure 43 the normal force is loaded on the beam by means of precise weights before the test is started and the load remains static until testing is completed. A design was need to be able to provide a dynamic load during the test. This design is shown in simplified form in figure 44 below, through the use of computer aided design (CAD) models. Each component will be discussed in full.

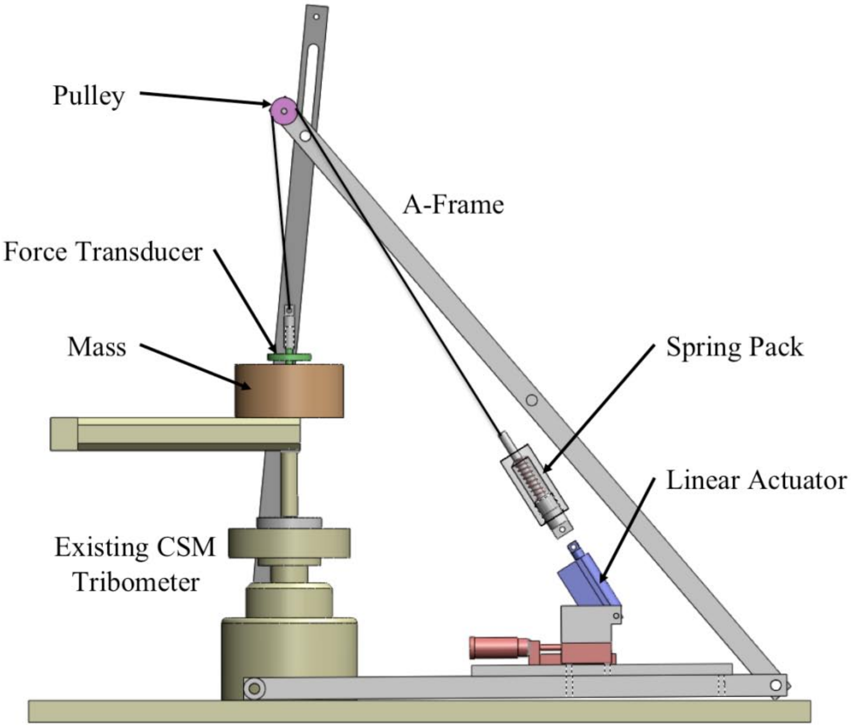

Figure 44 Variable force tribometer apparatus.

The basic idea in modifying the static load on the CSM tribometer is through application of Hookes Law, shown in equation 13 below:

$$F_s = -kx \tag{13}$$

where:

F_s is the spring force [N];

k is the spring constant [N/m];

x is the spring compression distance [m].

The design uses a linear actuator to cause the displacement of a spring, providing an opposing force to the mass through braided polymer line, in turn creating less force on the pin.

6.2.1. **Polymer Tension Line**

A braided polymer fishing line (0.12mm diameter) was used as tension line between the mass and linear actuator. The line has an eight-pound failure load. The tensile strength is equivalent to approximately 1.5 GPa, a value common to many monofilament polymer fibers. In the braided condition it is considered to have little or no "stretch" under load.

6.2.2. **Linear Actuator**

The Linear Motion Series PQ-12 actuator from Fergelli Technologies Inc. is a micro geared linear actuator. It is extended and retracted by 5 volts DC, and has a stroke of 20mm and a max rated force of 15N. It is capable of feedback position control through an on board linear potentiometer. This function could be used for precise control of the spring force, but is currently not being used. The actuator is also mounted on a manually adjustable slide to provide precise tension in the polymer line before testing. At peak efficiency, the load can be changed at a rate of 4.4 N/s.

6.2.3. **Spring Pack**

The spring pack is designed using a typical spring plunger system. As the plunger and body are pulled apart, the internal spring is compressed, offering resistance.

It is designed out of polyoxymethylene (Delrin) polymer doped with Polytetrafluoroethylene (Teflon) for lower sliding resistance. The spring is critical to the design of the system and must be tailored to the mass used for the test. The variable loading tribometer was designed to around a 7N mass. For this reason, and the limited amount of travel in the linear actuator, a spring constant of 0.63 N/mm was chosen. Theoretically, this allows the full 7N mass to be completely suspended with 11 mm of travel from the actuator. The extra travel will account for friction, line stretching, and component force effects.

The spring pack also adds for adjustability in the “resolution” of the applied force. As an example, a spring with a larger spring constant would allow for coarser adjustment of dynamic load, but at a faster rate. A spring with lower spring constant would allow finer adjustment of static force.

6.2.4. **Pulley**

The pulley used was a nylon body mounted on a roller bearing. The nylon was chosen for the lowest sliding friction with polymer tension line.

6.2.5. **Force Transducer**

A Dytran 1051V2 dynamic force transducer has been mounted directly in-line with the mass to ensure an accurate static load during testing. As mentioned above, certain factors will affect the accuracy of the load including; stretching of the braided polymer line, displacement of the a-frame, a non-vertical alignment between the mass and pulley, and the constant non-vertical alignment between linear actuator and spring pack adding a component of vertical force that counteracts the applied spring force.

6.2.6. **Mass**

The mass has been machined out of carbon steel (to dimensions that give an approximate mass of 7N).

6.2.7. **A-Frame**

An a-frame fixture was designed and manufactured out of 6061 T-6 aluminum. 6061 T-6 aluminum is often used in aerospace design for its high strength and low weight. Since this was to be a fixture added to the CSM tribometer, the A-frame needed to relatively stiff and rigid as compared to the elastic beam. Any extraneous movement in the variable loading a-frame during testing would translate to great error when determining the frictional force of the sample.

For this reason, a finite element analysis (FEA) was done on the A-Frame under a 7N loading to determine maximum stress and displacement conditions of the frame. The stress and displacement results are shown below in figures 45 and 46.

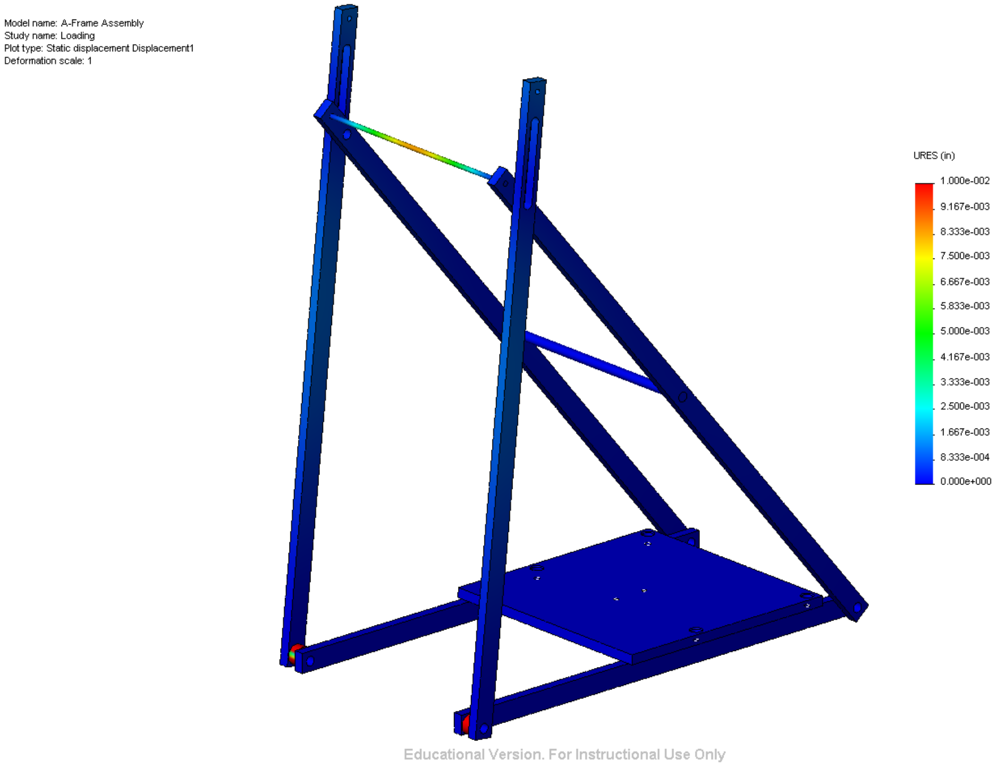

Figure 45 Finite element analysis displacement results for variable tribometer a-frame.

The large displacement elements are plotted closer to red while the lower displacement elements are plotted closer to blue. The approximate color and displacement values are shown in the key. The highest displacement was in the 3 mm diameter bean suspending the mass. The total displacement in the beam was 0.20mm. This value is considered acceptable as it is in the downward direction and should not affect any tangential forces.

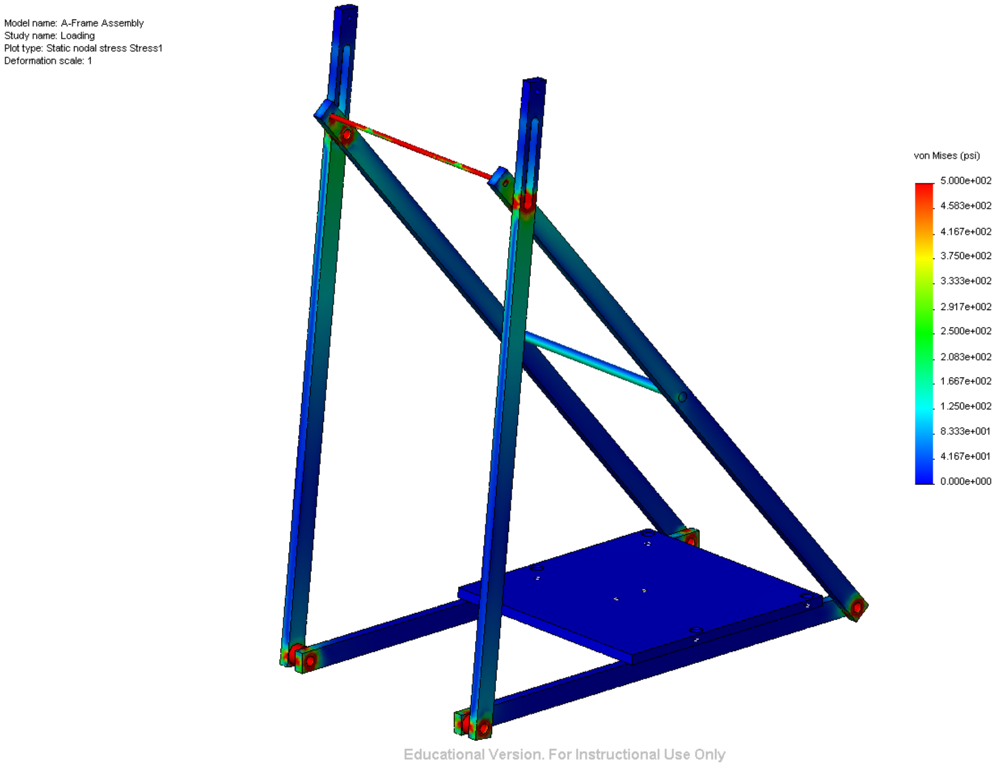

Figure 46 Finite element analysis stress results for variable tribometer a-frame.

The high stress elements are plotted closer to red while the lower stress elements are plotted closer to blue. The approximate color and displacement values are shown in the key. The highest stress in the a-frame was approximately 24 MPa, locating on the top and bottom of the beam supporting the mass. The yield stress for 6061 T-6 aluminum is approximately 255 MPa. The stresses in the structure are an order of magnitude lower than yielding and therefore the a-frame can be considered extremely stiff. There should be no considerable affect on tangential forces.

6.3. Setup

Figure 47 shows the current tribometer setup for experimentation.

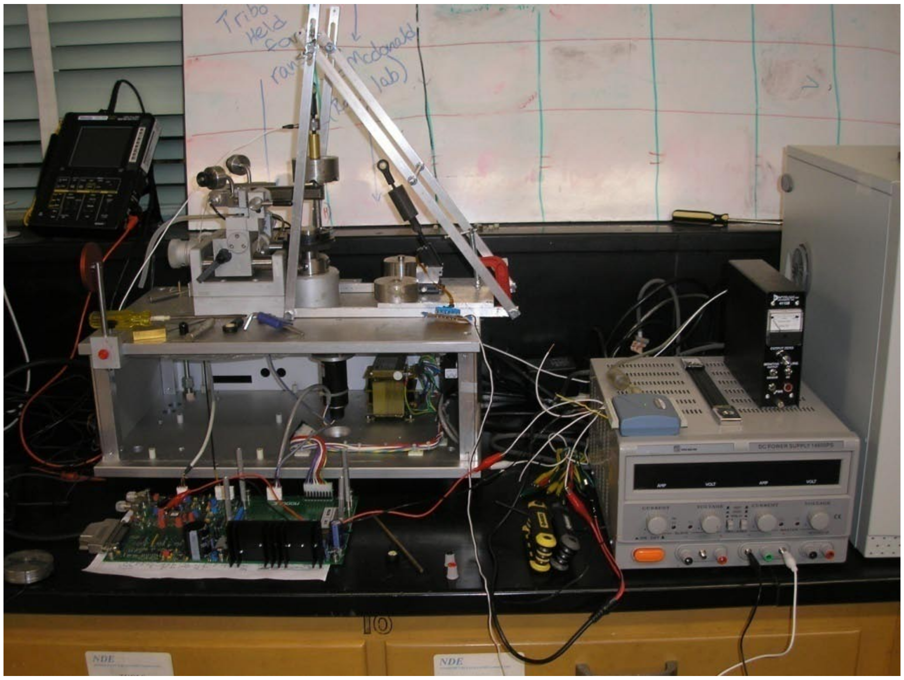

Figure 47 Variable force tribometer experimental set-up.

The operational parameters of the tribometer are summarized in table 17.

Table 17 Summary of operational parameters for the dynamic tribometer.

Parameters	Range of Measurements
Load (N)	0 – 7*
Loading Rate (mm/s)	Linear speed = -0.6(Voltage) + 12
Electrical Contact Resistance Ω	N/A
Velocity (m/s)	0.01- 0.06

* wider load range available.

6.4. Dynamic Friction Testing

Dynamic load testing was accomplished using the variable force tribometer. A MPJA DC power supply was used to control the displacement and speed of the PQ-12 linear actuator and corresponding normal force on the tribometer pin. All other testing variables were controlled using the CSM Tribox software.

6.4.1. **Calibrations**

Measurements of normal force during testing were accomplished using a Dytran 1051V2 dynamic force transducer and Measurements Computing USB – 1208FS data acquisition system (DAQ). Control of the DAQ as well as signal processing was done using LABVIEW software. The normal force was calibrated between two points;

completely unloaded and fully loaded in tension with a 7N mass. The calibration curve for normal load is shown in figure 48 below.

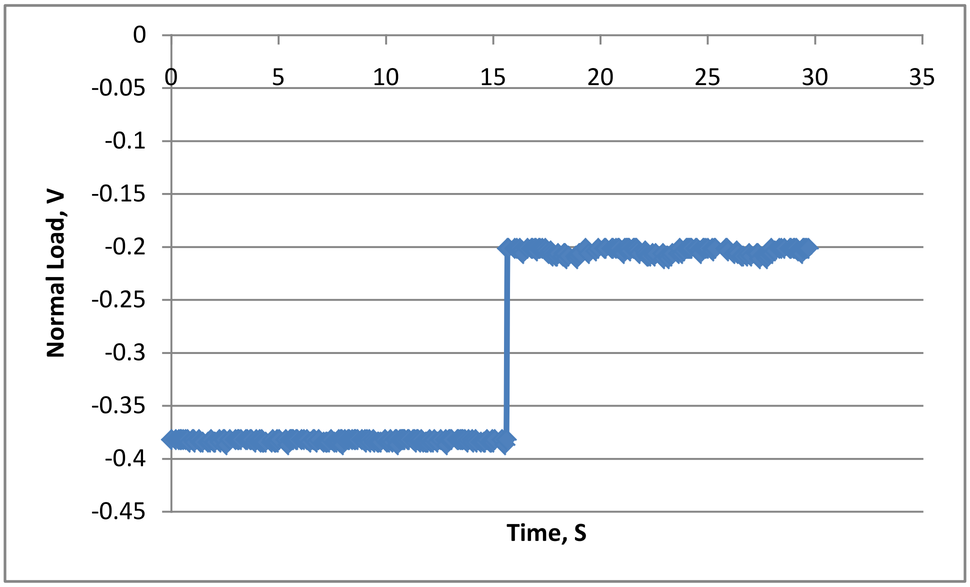

Figure 48 Calibration curve for normal load.

The signal from the force transducer is shown in blue. There is some discrepancy in the force transducer readings as it is primarily designed for dynamic loading conditions and therefore can only give reasonable data in quasi-static equilibrium conditions for a short period of time. The empirical relationship between the transducer signal voltage and load is shown in equation 14 below:

$$F_n = 41.698 \cdot V + 15.62 \qquad (14)$$

where

F_n is the normal force[N];

V is the signal voltage [V].

Tangential force measurements were done by utilizing the current sensor system embedded in the CSM Tribometer. The signal from a linearly variable differential transformer measuring tangential deflection of the elastic pin holder was tapped into and then calibrated with masses for tangential load measurements using the DAQ. The calibration curve is pictured in figure 49 below.

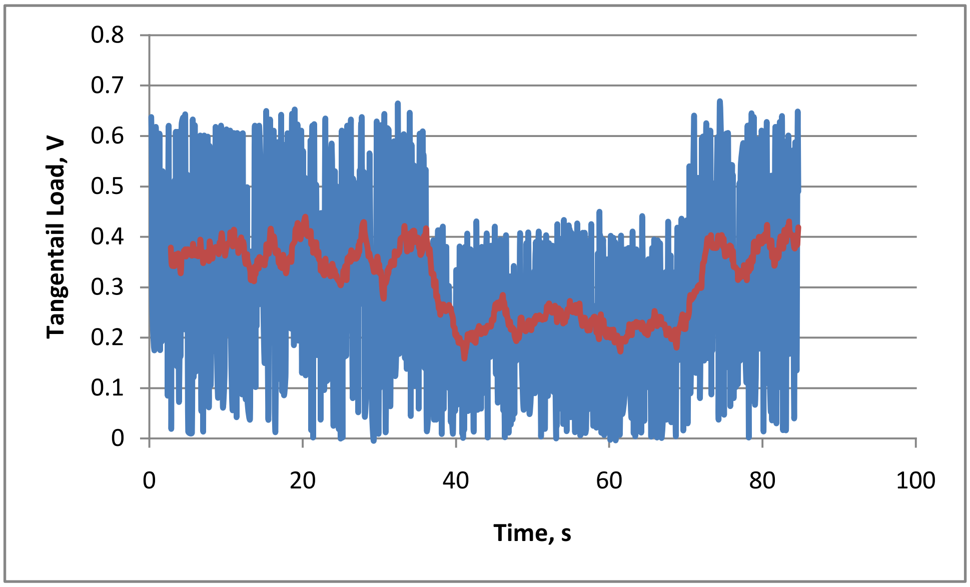

Figure 49. Calibration curve for tangential load.

The half amplitude for the raw tangential load signal can be seen by the blue line in the figure above. The signal was then filtered using a moving average as shown by the red line above. With no load on the beam the signal reads approximately 3.5 Volts (on average). When a 3N load is applied to the beam (in the tangential direction) the signal drops to approximately 2.5 Volts. Due to the sensors linearity, the empirical relationship between voltage and load was calculated and shown in equation 15 below:

$$F_t = -21.28 \cdot V + 7.82 \qquad (15)$$

where

F_t is the tangential force [N];

V is the signal voltage [V].

6.4.2. **Testing**

Inconel 625 alloy was chosen as the test countersufrace for preliminary dynamical loading experiments using the variable force tribometer. The material was chosen in supplement to the extensive tribological characterization done in previous sections. For the initial dynamic experiments, the Inconel 625 test sample was similar in properties and preparation to the samples discussed in detail earlier in this thesis (REF Table 5). Similarly, a 6 mm AISI 440C matensitic stainless steel ball bearing was used for the tribological pin material. Testing was done at a speed of approx. 2 cm/s. This was controlled using the onboard CSM software.

The results for initial friction testing can be seen in figure 50 below.

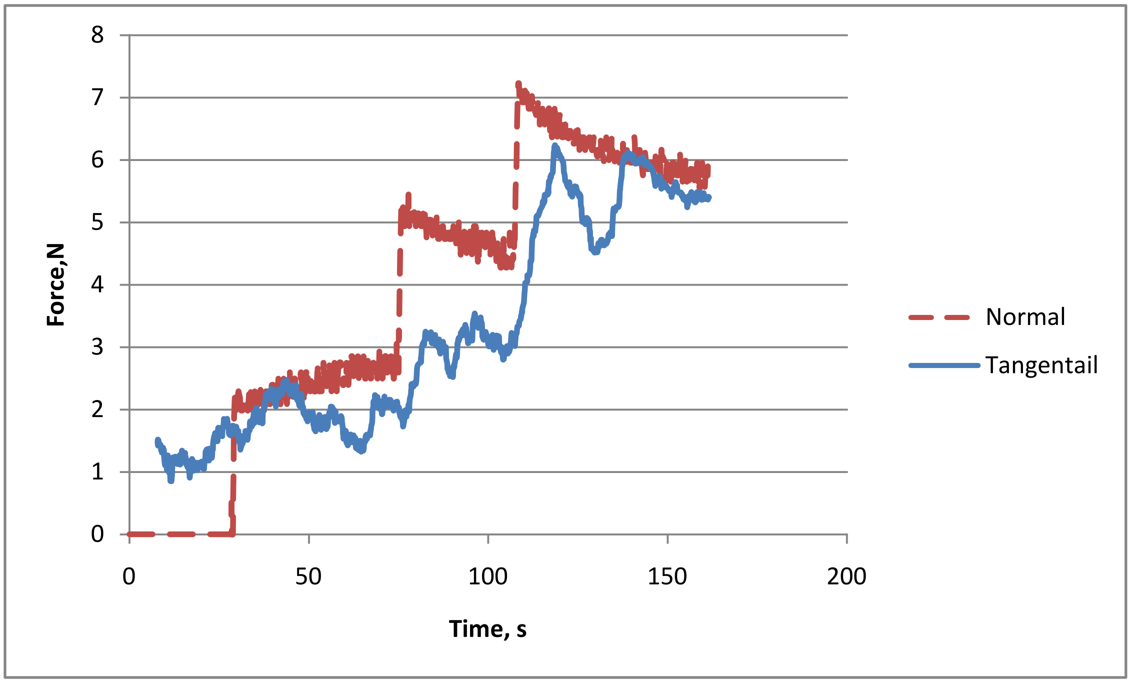

Figure 50. Dynamic load response of Inconel alloy 625.

In the figure above we see the applied normal load (red-dashed) and the corresponding tangential load response (blue). Three observations can be immediately made of the loading behavior. First, the normal load seems to show a trend to slightly lower after every heightened application. Part of this behavior could be a result of the quasi-static nature of the load cell, however it is important to note that from a tribological standpoint, as more load is applied the true contact area will change, corresponding to a change in the contact area undergoing wear. Therefore, the downward trend in normal force could also be a indication of a wear induced change in sliding contact area in the wear track, leading to a slightly lower applied normal load.

The second observation simply demonstrates what has been shown by Leonardo da Vinci and Guillaume Amontons[1]; the proportionality between normal load, and tangential load. Figure 50 clearly shows that with each increase in applied load, we see an increase in tangential load.

The third and most significant observation is of the truly dynamic nature of the tangential load. We see that while the tangential load increases proportionally with the applied load, it is in no means stagnant. The tangential load seems to initially vary greatly after the application of normal force. For example, we can see after the normal load is increased from 5N to 7N the tangential load increases proportionally and then rapidly decreases. After which it rises again and then stabilizes by the end of the test. The large fluctuations may be brought on by the onset of wear a change in the Inconel 625 wear mechanism (multi-modal to single modal) as discussed in section IV.

Figure 51 is similar to that of figure 50, however, the coefficient of friction has been added for comparison purposes.

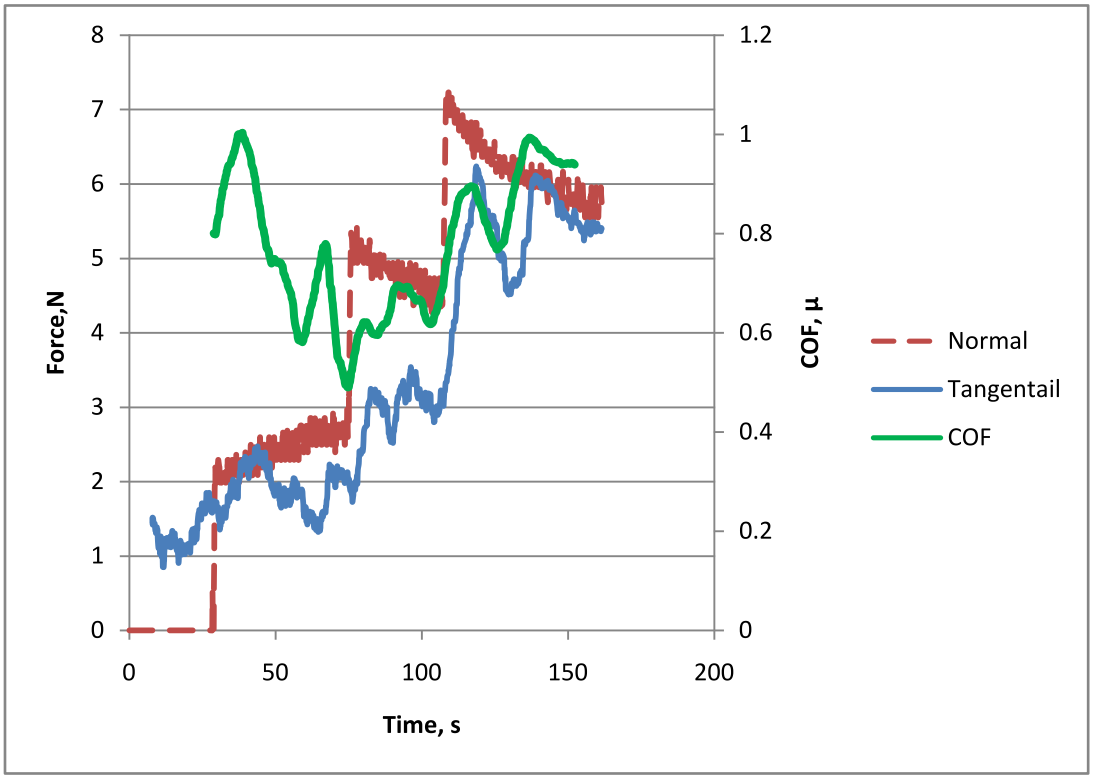

Figure 51 Dynamic load response of Inconel alloy 625 with coefficient of friction measurement.

We can see from the figure that the coefficient of friction (green) has been plotted with the dynamic load response for comparison purposes. It should be noted that the right-handed axis pertains only to the friction measurement. It is interesting to observe that the friction response is similar and proportional to that of the tangential load. This observation supports what has been previously mentioned for Inconel 625; the tangential load is dependent on the friction induced sliding conditions, between the pin and countersurface. From the first law of friction, we can then assume that the sliding conditions are also a function of the applied normal force. This preliminary experiment serves as a great example in demonstrating the realistic and dynamic nature of the first law of friction. It should also be noted that the values for coefficient of friction for Inconel alloy 625 are similar to what has previously been reported in this thesis.

6.5. Ending Remarks

In this section the engineering design of a variable force tribometer was shown in detail. In addition to pertinent design features, preliminary dynamic test results were discussed. The preliminary results have indicated the truly dynamic nature of the applied normal and resultant tangential loads during friction testing. The results have also fundamentally shown how these dynamic forces affect the friction coefficient. These early results utilizing the variable force tribometer will lay the groundwork for more advanced research into the dynamic nature of friction.

7. CONCLUSIONS AND FUTURE RECOMMENDATIONS

This section summarizes the results and states the significance and major conclusions of the research.

7.1. Conclusions

The research conducted in this thesis was done in three unique areas of tribology;: investigation of wear and friction in high-performance alloys, in situ observation of friction of micro structured materials, and the development of a novel tribometer for testing the dynamic frictional behavior of materials. The results have brought a new understanding in tribological properties and performance of high performance materials. Principles behind the evaluation of friction and wear characteristics in specialty engineering materials and designs were understood. This research has shown:

- Sliding friction and specific wear rate were found as a function of the frictional work. This indicates that the tribological properties of materials are process history related. The accumulation of energy effects altered the materials properties, which lead to the specific behavior in friction and wear. The frictional work has been shown as a good method to characterize the materials tribological behavior, as it’s a common mechanical engineering concept that can be readily understood.
- Spatially resolved in situ measurements of friction and electrical contact resistance have proven to be a powerful approach to observe the complex friction and wear phenomenon happening between sliding contacts. This method is able to record the friction history, giving the engineer an idea of the predictability in a sliding contact pair.

- Careful post-testing characterization indicated that complex material transferring mechanisms are involved during sliding. Such transfer affects not only the surface integrity (roughness), but also the contact area and electrical contact resistance. This observation is important for understanding the MEMS failure mechanisms.
- A novel apparatus has been developed in order to test the tribological response of materials under dynamic tribometer testing.

7.2. Research Impacts and Applications

Three examples are given below to show the importance of the present research.

Understanding friction and wear response as a function of input work has been proven to be a very important tool for tribologists and engineers, particularly when little tribological testing data exists. “Frictional work”, is a good way to give a baseline response for the material in a tangible way all engineers can understand. This is even more important in today’s industry when high-performance materials are being used more often; sometimes in non-traditional tribological systems. One such system is the Crew Impact Attenuation (CIA) system on the NASA Orion spacecraft. The Orion spacecraft is the new transport capsule designed to shuttle astronauts safely to and from the space station and ultimately, the moon. To ensure the astronauts make a return to earth, engineers much account for many different variables, including the impact of landing. To mitigate this impact, engineers have developed a friction shock attenuator. The attenuator uses the friction between a series of metallic diaphragms and an Inconel alloy strut to absorb landing impact. When engineers attempted to evaluate the tribological performance of the friction materials in the design there were no baselines or comparable studies.

In situ examination or monitoring of friction and wear has immense practical applications. Sliding contact between two real bodies is a difficult process to model in its own, much less with any accurate prediction of wear. With an immediate understanding of how the known variables in a tribosystem influence the outcome effects, an engineer may gain a better understanding on how to design a system for the unknown contact conditions. This has important practical applications, particularly to MEMS. Due to the inherent nature of working in a micro scale, MEMS must be designed to very high tolerances. In these systems, any significant wear between the MEMS elements could potentially result in failure of the system; either through altered contact mechanics or interaction with wear debris. At this scale, ordinary lubricants cannot be used to reduce friction or stiction[51]. Accurate and simple in situ monitoring of friction and wear could be extremely beneficial to the MEMS researcher and designer.

Finally, understanding the tribological response to a series of dynamic conditions through the use of electrical contact resistance can provide a multitude of uses to a tribologist. As an example, it has been mentioned before that the electrical contact resistance between two materials is related to their true contact. This remains true while sliding. Currently there is no measure of true contact pressure while sliding. A combination of dynamic loading and electrical contact resistance may provide clues to the real-time nature and behavior of the true contact pressure.

7.3. Future Work

Development will continue in the integration of in situ electrical contact resistance monitoring to the dynamic loading tribometer. Additionally, an ASTM standard could be developed for the dynamic load testing. In situ microscopic monitoring coupled with in situ ECR measurements could also provide an additional level of wear information to tribology.

REFERENCES

1 D. Dowson, *History of Tribology* (Longman Group Limited London, 1979).

2 G. W. Stachowiak, A. W. Batchelor, and G. B. Stachowiak, *Experimental Methods in Tribology*, Vol. 44 (Elsevier, Amsterdam, 2004).

3 R. G. Bayer, *Engineering Design for Wear*, Vol. 176, 2nd ed. (Marcel Dekker, Inc. , New York 2004).

4 P. Winiwarter and C. Cempel, Systems Research **9**, 9-34 (1992).

5 G. W. Stachowiak and A. W. Batchelor, *Engineering Tribology,* Third ed. (Elsevier, Oxford, 2005).

6 D. Tabor, *Tribology International* **28**, 7-10 (1995).

7 R. J. Forbes, *Man the Maker: A History of Technology and Engineering* (Henry Schuman, New York 1950).

8 B. L. E. W. Group, "Lubrication (Tribology) Education and Research. A Report on the Present Position and Industry's Needs". http:// www.opsi.gov.uk; (The Office of Public Sector Information, formerly Her Majesty's Stationary Office, London, England,1966).

9 K. K. Papok, *Chemistry and Technology of Fuels and Oils* **7**, 154-158 (1971).

10 *ASTM Book of Standards*, Vol. 03.02 (ASTM International, West Conshohocken, PA, 2009).

11 L. Euler, *Memoires de l'academie des sciences de Berlin* **4**, 122-132 (1750).

12 R. G. Bayer, *Mechanical Wear Fundamentals and Testing,* Second ed. (Marcel Dekker, New York, 2004).

13 K. Kato, *Classification of Wear Mechanisms/Models* (John Wiley & Sons Ltd. , West Sussex, England, 2005).

14 D. H. Buckley, *Surface Effects in Adhesion, Friction, Wear, and Lubrication.* (Elsevier Scientific, New York, 1981).

15 J. A. Williams, *Engineering Tribology* (Oxford Press, New York, 1994).

16 S. B. Sakrani and J. L. Sullivan, in *Third International Conference on Thin Film Physics and Application*; *Vol. 3175* (SPIE, Shanghai, China, 1998), p. 157-179.

17 K. A. Heck, J. S. Smith, and R. Smith, *Journal of Engineering for Gas Turbines and Power* **120**, 363-369 (1998).

18 W. F. Smith, *Structure and Properties of Engineering Alloys* (McGraw-Hill, New York, 1981).

19 K. P. Cooper, *J. Vac. Sci. Technol.* **A 4**, 2857-2861 (1986).

20 P. K. Aw, A. W. Batchelor, and N. L. Loh, *Surface Coatings & Technology* **89**, 70-76 (1996).

21 J. A. Laskowski and C. Dellacorte, *Lubrication Engineering* **52**, 605-612 (1996).

22 M. K. Lim, S. D. Oh, and Y. Z. Lee, *Nuclear Engineering and Design* **226**, 97-105 (2003).

23 R. Maboudian, W. R. Ashurst, and C. Carraro, *Tribology Letters* **12**, 95-100 (2002).

24 B. Buhushan, *Journal of Engineering Tribology* **215**, 1-18 (2005).

25 F. L. S. Tai Y.C., Muller R.S., in *IC-processed Micro-motors: Design, Technology, and Testing* (IEEE, New York, 1998), p. 1-6.

26 D. M. Tanner and M. T. Dugger, in *Wear Mechanisms in a Reliability Methodology* (SPIE, San Jose, CA 2002).

27 D. Wang and K. Kato, *Wear*, 519-526 (2002).

28 M. P. d. Boer, N. F. Smith, N. D. Masters, M. B. Sinclair, and E. J. Pryputniewicz, in *Integrated Platform for Testing MEMS Mechanical Properties at the Wafer Scale by the IMap Methodology* (ASTM, Orlando, FL, 2000).

29 A. P. Merkle and L. D. Marks, *Wear* **265**, 1864-1869 (2008).

30 S. Ingole, A. Schwartzman, and H. Liang, *Journal of Tribology* **129**, 11-16 (2007).

31 T. Tamai, *IEICE Trans. Electron* **E89**, 1122-1128 (2006).

32 *Inconel Alloy 625*.Technical Bulletin: SMC-063, (Special Metals Corporation, New Hartford, NY, 2006).

33 Retrieved from *http://www.specialmetals.com/products/inconelalloy625.php*; September 8, 2008. (Special Metals Corporation, New Hartford, NY, 2006).

34 Retrieved from *http://www.specialmetals.com/products/inconelalloyhx.php;* September 8, 2008. (Special Metals Corporation, New Hartford, NY, 2006).

35 Y. Sun, T. Bell, and G. Wood, *Wear* **178**, 131-138 (1994).

36 Custom Order Specifications. Retrieved from *www.winball.com;* September 16, 2008 (Winsted Precision Ball, Winsted, CT, 2004).

37 Materials Used for balls. Retrieved from *http://www.precisionballs.com/tech_papers.html;*September 16, 2008 (Bal-tec, Los Angeles, 2008).

38 E. Oberg, F. D. Jones, H. L. Horton, and H. H. Ryffel, *Machinery's Handbook*, 25th ed. (Industrial Press Inc. , New York, 1996).

39 johnh; Retrieved from *http://microscopy.tamu.edu/instruments/scanning-electron-microscopy/*, February 17, 2008.

40 ASTM, in *Wear and Erosion*; *Vol. G 99 - 05* (ASTM International, West Conshohocken, PA, 2005).

41 Vol 1 - Properties and Selection: Irons, Steels, and High Performance Alloys. *Metals Handbook*, 10th ed. (ASM International, West Conshohocken, PA 2002).

42 A. W. Ruff, *Typical Properties of Sliding Contact Materials* (CRC Press LLC, Boca Raton, 1997).

43 Vol 2 - Properties and Selection: Nonferrous Alloys and Special-Purpose Materials. *Metals Handbook*, 10th ed. (ASM International, West Conshohocken, PA, 2002).

44 Retrieved from *http://www.zygo.com/?/met/profilers/newview600/;* March 20, 2008 (Zygo Corporation, Middlefield, CT, 2007).

45 K. Holmberg and A. Matthews, *Tribology of Engineered Surfaces* (John Wiley & Sons Ltd., West Sussex, England, 2005).

46 S. M. Hsu, R. G. Munro, M. C. Shen, and R. S. Gates, *Boundary Lubricated Wear* (John Wiley and Sons, Ltd. , West Sussex, England, 2005).

47 V. V. Dunaevsky, *Friction and Wear Equations* (CRC Press LLC, Boca Raton, 1997).

48 B. B. Venkatsan V., *Wear* **171**, 25-32 (1994).

49 R. Holm, *Electric Contacts Handbook*, 3rd ed. (Springer-Verlag, Berlin, 1958).

50 J. A. Williams and H. R. Le, J*ournal of Physics D: Applied Physics* **36**, R201-R214 (2006).

VITA

Name: Grant Robert Fox

Address: Department of Mechanical Engineering

c/o Dr. Hong Liang

Texas A&M University

College Station, TX 77845-3123.

Email Address: grant.r.fox@gmail.com

Education: B.S., Mechanical Engineering, University of New Mexico, 2005

M.S., Mechanical Engineering, Texas A&M University, 2009